Inferring Telescope Polarization Properties Through Spectral Lines Without Linear Polarization

Alysa Derks
Department of Astrophysical and Planetary Sciences
University of Colorado, Boulder

Thesis Advisor: Valentin M. Pillet, APS
Honors Council Representative: Erica Ellingson, APS
Other Committee Members: Kelvin Wagner, ECEN
Christian Beck, National Solar Observatory

Defended: April 10, 2017

1 Abstract

Polarimetric observations taken with ground- or space-based telescopes usually need to be corrected for changes of the polarization state induced in the optical path. In this paper, I present a new technique to determine the polarization properties of a telescope through observations of spectral lines that have no or negligible intrinsic linear polarization [1] signals. For such spectral lines, any observed linear polarization must be induced by the telescope optics. I apply the technique to observations taken with the Spectropolarimeter for Infrared and Optical Regions (SPINOR) at the Dunn Solar Telescope (DST) and demonstrate that I can retrieve the characteristic polarization properties of the DST at three selected wavelengths of 459, 526 and 615 nm. I determine the amount of cross-talk between the intensity, Stokes I, and the linear and circular polarization [2] states, Stokes Q, U and V, and between Stokes V and Stokes Q and U in spectropolarimetric observations of active regions on the solar surface. I fit a set of parameters that describe the polarization properties of the DST to the observed cross-talk values [3]. I compare my results to parameters that were derived using a conventional telescope calibration unit (TCU). The values for the ratio of reflectivities $X = r_s/r_p$ [4] and the retardance τ of the DST turret mirrors from the analysis of the cross-talk match those derived with the TCU within the error bars. I find a negligible contribution of retardance from the entrance and exit windows of the evacuated part of the DST. Residual cross-talk after applying a correction for the telescope polarization stays at a level of 3-10 % regardless of which parameter set is used, but with an rms fluctuation in the input data of already a few percent. The accuracy in the determination of the telescope properties is thus more limited by the quality of the input data than the method itself. It is possible to derive the parameters that describe the polarization properties of a telescope from observations of spectral lines without intrinsic linear polarization signal. Such spectral lines have a dense coverage (about every 50 nm) in the visible part of the spectrum (400–615 nm), but none were found at longer wavelengths. Using spectral lines without intrinsic linear polarization is a promising tool for the polarimetric calibration of current or future solar telescopes such as the Daniel K. Inouye Solar Telescope (DKIST).

[1] linear polarization = light in the form of a plane wave

[2] circular polarization = light composed of two plane waves of equal amplitude, differing in phase by 90 deg.

[3] polarization cross-talk is spurious polarization signal caused by transfer from one Stokes parameter into another one by polarimetrically active optical elements

[4] r_s is the reflectivity in the plane perpendicular to the plane of incidence. r_p is the reflectivity in the plane parallel to the plane of incidence.

Contents

2 Introduction

Measuring the polarization state of light, or polarimetry, is important because we can use these observations to better protect ourselves from solar flares. Incoming light from the sun is unpolarized. Some telescope optics can change this, creating polarization and making observers see a polarization that shouldn't really be there. Therefore, this induced telescope polarization needs to be determined and compensated for.

Most existing solar telescopes were designed without clear requirements about their polarimetric performance and calibration. The telescopes currently available for high spatial resolution solar physics are calibrated using an analytical model of their time-varying Mueller matrices [5]. The free parameters in these models are fit to data obtained using calibration polarizers at the entrance of the telescopes (Skumanich et al. (1997); Beck et al. (2005); Selbing (2010); Socas-Navarro et al. (2011)) or they used literature values for the polarization properties of the mirrors (see Collados (1999); Schlichenmaier & Collados (2002)).

The calibration strategy of the Advanced Stokes Polarimeter (ASP; Elmore et al. 1992) at the Dunn Solar Telescope (DST Dunn 1964; Dunn & Smartt 1991) as described in Skumanich et al. (1997) paved the way for other telescopes to carry out similar polarimetric characterizations. A key aspect of the ASP/DST calibration was to split the polarization effects of the telescope with a time-dependent Mueller matrix $\mathbf{T}(t)$ and those of the polarimeter with a static Mueller matrix $\mathbf{X}$ by inserting polarization calibration optics between the two. This point of insertion made the polarimeter matrix $\mathbf{X}$ constant in time but made the telescope Mueller matrix $\mathbf{T}$ time-dependent to account for the varying telescope geometry. The calibration optics provided the polarization properties of all of the optical components downstream from the insertion point, i.e., the polarimeter matrix. Upstream from the insertion point, the data obtained with the entrance polarizer constrained the polarization properties described by the matrix $\mathbf{T}(t)$. Polarization calibration optics usually have a small diameter and can be manufactured to high accuracy compared to the large optics used for the entrance polarizers. Placing such high-quality calibration optics as high up in the optical path as feasible is thus beneficial.

All modern solar telescopes adopted the strategy of the ASP and incorporated calibration optics as early in the optical path as possible, thus calibrating the largest number of optical components. One recent example is the German GREGOR telescope (Schmidt et al. 2012) that uses a polarization calibration unit near the secondary focus of the telescope, right after the primary and secondary mirrors. The calibration unit is located before breaking the revolution symmetry around the optical axis. Thus, the expected polarization effects from the mirrors upstream are small, originating only from the off-axis configuration outside the center of the field of view, and from diffraction effects. Sanchez Almeida & Martinez Pillet (1992) demonstrated that these effects are only important for absolute polarimetry at the 10^{-4} level. For GREGOR, the matrix downstream of the calibration optics is geometry and time-dependent, whereas the matrix upstream is constant in time and, in this case, close to the identity matrix.

The Daniel K. Inouye Solar Telescope (DKIST; McMullin et al. 2016) under construction on the island of Maui will follow a similar strategy as GREGOR. A polarization calibration unit is located downstream of the secondary mirror. In the case of DKIST, the first two mirrors M1 and M2 (see Fig. 1) have an off-axis configuration that generates a telescope matrix $\mathbf{T}$ that deviates significantly from the identity matrix, and is constant in time. The angles of incidence of these two mirrors vary from 12 to 14 degrees and non-diagonal matrix elements of a few 10^{-2} are expected. Accurate ray-tracing with realistic modeling of the mirror coatings demonstrates that Stokes $U \leftrightarrow V$ cross-talk

[5] a 4×4 matrix that holds the polarization properties of a telescope.

terms on the order of 8% can be expected in **T** (Harrington & Sueoka 2016, 2017). Interestingly, the same calculations show that the diagonal elements are all close to unity to within less than a percent. Similar to GREGOR, all time dependencies are transferred to the matrix downstream of the calibration optics. The polarization properties of **T** are independent of the telescope pointing and change only with the degradation of the coatings with time. Thus, the inference of this matrix is much simpler than in the case of the DST.

The 4-m aperture of DKIST makes it impossible to use an entrance linear polarizer. A number of strategies have been devised to calibrate the instrumental polarization to the required level of accuracy of 5×10^{-4} (see Socas-Navarro et al. 2005; Socas-Navarro 2005a,b; Elmore et al. 2014). One option for the calibration of the DKIST **T**-matrix is based on spectral lines that have no intrinsic linear polarization through the Zeeman effect, e.g., the Fe II line at 614.9 nm (Lites 1993). A list of lines with this property, which depends on the atomic transitions involved, was compiled by Sanchez Almeida & Vela Villahoz (1993) and Vela Villahoz et al. (1994). These authors proposed the use of those lines to measure the asymmetries of their Stokes V profiles as they are unaffected by instrumental polarization. In this paper, I revisit their list of lines without linear polarization to study their suitability for polarimetric calibration. I compare the results obtained from observations of lines without linear polarization taken in 2016 at the DST to those from the standard calibration done in 2010 using the telescope entrance linear polarizers to understand the limitations of the approach. The calibration of the $\mathbf{T}(t)$ matrix for the DST is more complex than the calibration of **T** for DKIST, thus succeeding with the DST demonstrates the potential interest of this method for DKIST. This approach was first proposed for DKIST by Socas-Navarro et al. (2005) who demonstrated that it can potentially achieve the required accuracy.

Section 3 describes my selection process to identify suited spectral lines. Section 4 gives the theoretical background for the derivation of telescope properties from observations. The observations used are described in Section 5. Sections 6 and 7 provide the data analysis and results, respectively. Section 8 contains the discussion, while Section 9 gives my conclusions. The appendices provide the complete line list and a few more data examples at other wavelengths.

3 Synthesis of Spectral Lines and Line Selection

There exist special atomic transitions that produce spectral lines without any, or with negligible, intrinsic linear polarization (LP) induced by the Zeeman effect (Sanchez Almeida & Vela Villahoz (1993); Vela Villahoz et al. (1994)). These lines can be used to uncover polarization properties of a telescope or to test the quality of the polarimetric calibration because most linear polarization signal is spurious and indicates polarization cross-talk. I analyzed the two tables of spectral lines without or with small LP provided by Vela Villahoz et al. (1994, their Tables 1 and 2) to find the lines that would be best suited for telescope calibration purposes. I restricted the analysis to lines with a rest wavelength from 400–1100 nm. I obtained all necessary information including excitation potential, log(gf)[6], transition parameters, and the effective Landé coefficient ($g_{\rm eff}$)[7] from the NIST Atomic Spectral Database[8]. I disregarded any lines for which the value of log(gf) could not be found. This left 31 lines from Table 1 of Vela Villahoz et al. (1994) (see Table 4) and 56 lines from their Table 2 (see Table 5).

After the suitable lines were chosen, a spectral synthesis was done using the Stokes Inversion

[6] the logarithm of the multiplicity of the level times the oscillator strength, respectively.

[7] measures the reaction of an electron transition to magnetic fields.

[8] http://physics.nist.gov/PhysRefData/ASD/lines_form.html

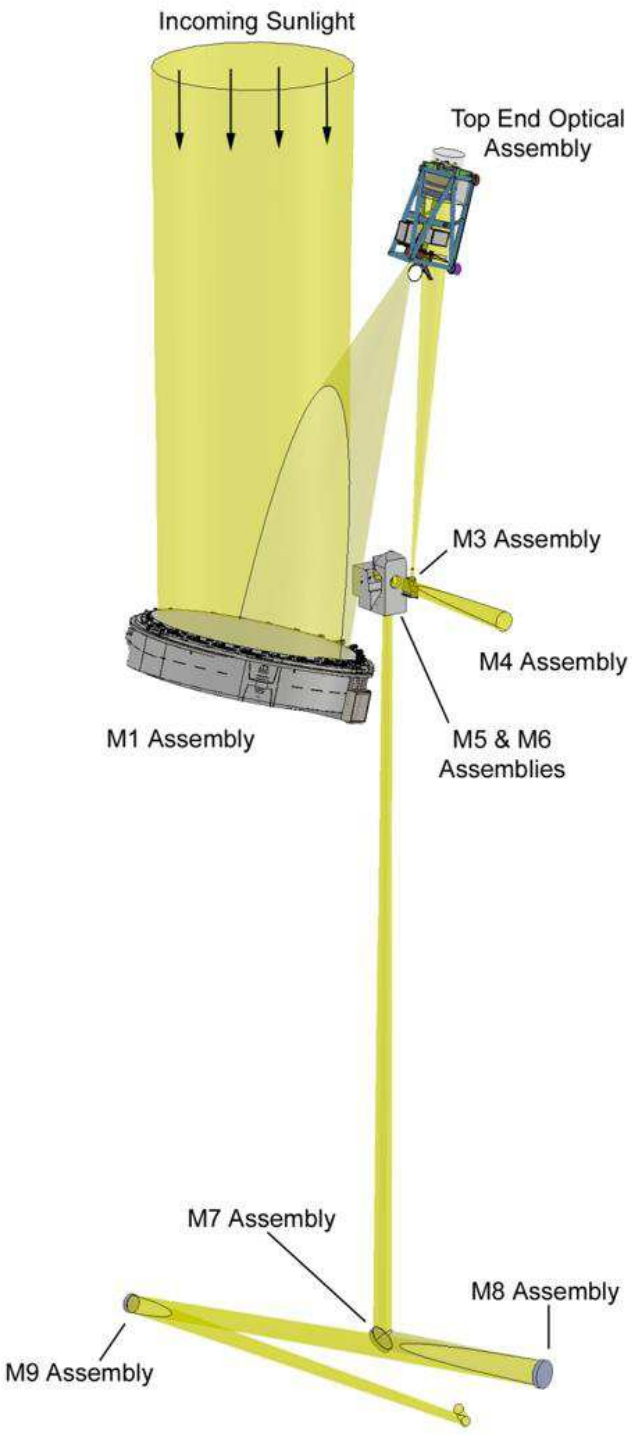

Figure 1: A schematic of the DKIST telescope.

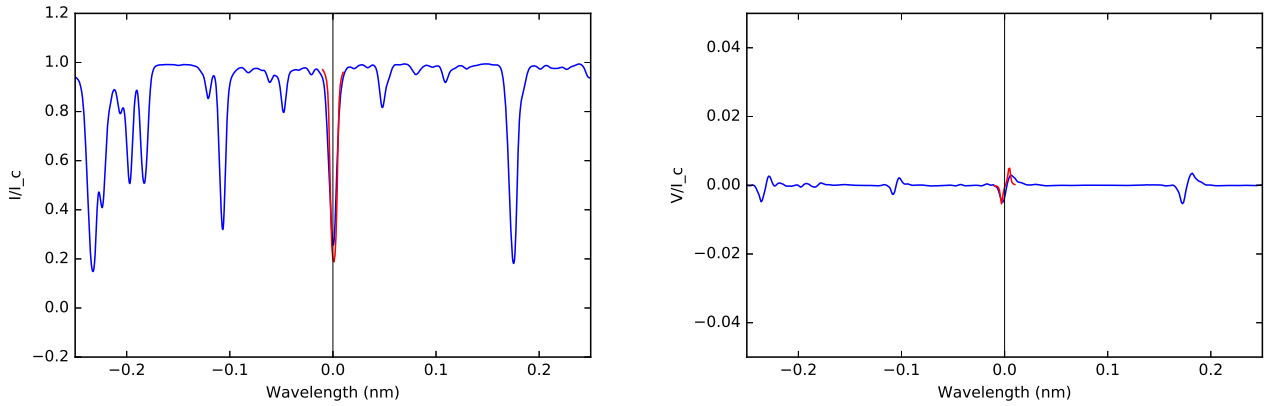

Figure 2: Synthetic Stokes profiles of Stokes I (left panel) and V (right panel) for the Cr II line at 458.820 nm in the synthesis with 1500 G are shown in red. The blue lines show the corresponding profiles from the FTS atlas.

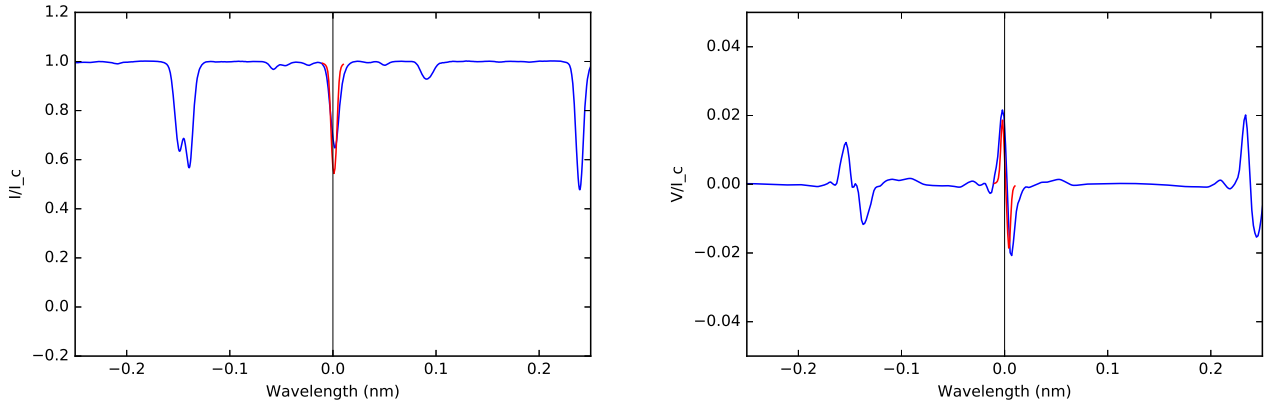

Figure 3: Same as Fig. 2 for Fe II at 614.923 nm.

based on Response functions code [9] (SIR; Ruiz Cobo & del Toro Iniesta 1992). For this synthesis, I used a solar model atmosphere with a magnetic field inclination of 45 ° and an azimuth of 22.5 °, a macro- and micro-turbulent velocity of 1 km s^{-1}, and zero Doppler shift. The magnetic field inclination and azimuth were chosen in order to obtain polarization signal in all Stokes parameters Q, U, and V (without these specifications, only I and V signals would have been produced), whereas the macro- and micro-turbulence were chosen so that realistic polarization amplitudes would be obtained. The synthesis was repeated with three different magnetic field strengths: 100 G (quiet Sun), 1500 G (plage), and 2500 G (sunspot) to simulate regions of different magnetic activity on the solar surface.

Using the synthetic profiles, I made a final selection of lines suitable for calibration purposes based on line depth, polarization amplitude, and absence of line blends. Line blends were identified by a comparison to spectra from the Fourier Transform Spectrometer Atlas (FTS; Kurucz et al. 1984). I extracted the line depths from the 100 G synthesis, and the maximal Stokes Q, U, and

[9] SIR synthesizes spectral lines formed in the presence of magnetic fields. It calculates the Stokes Spectra emerging from any specified model atmosphere by numerically solving the radiative transfer equation for polarized light.

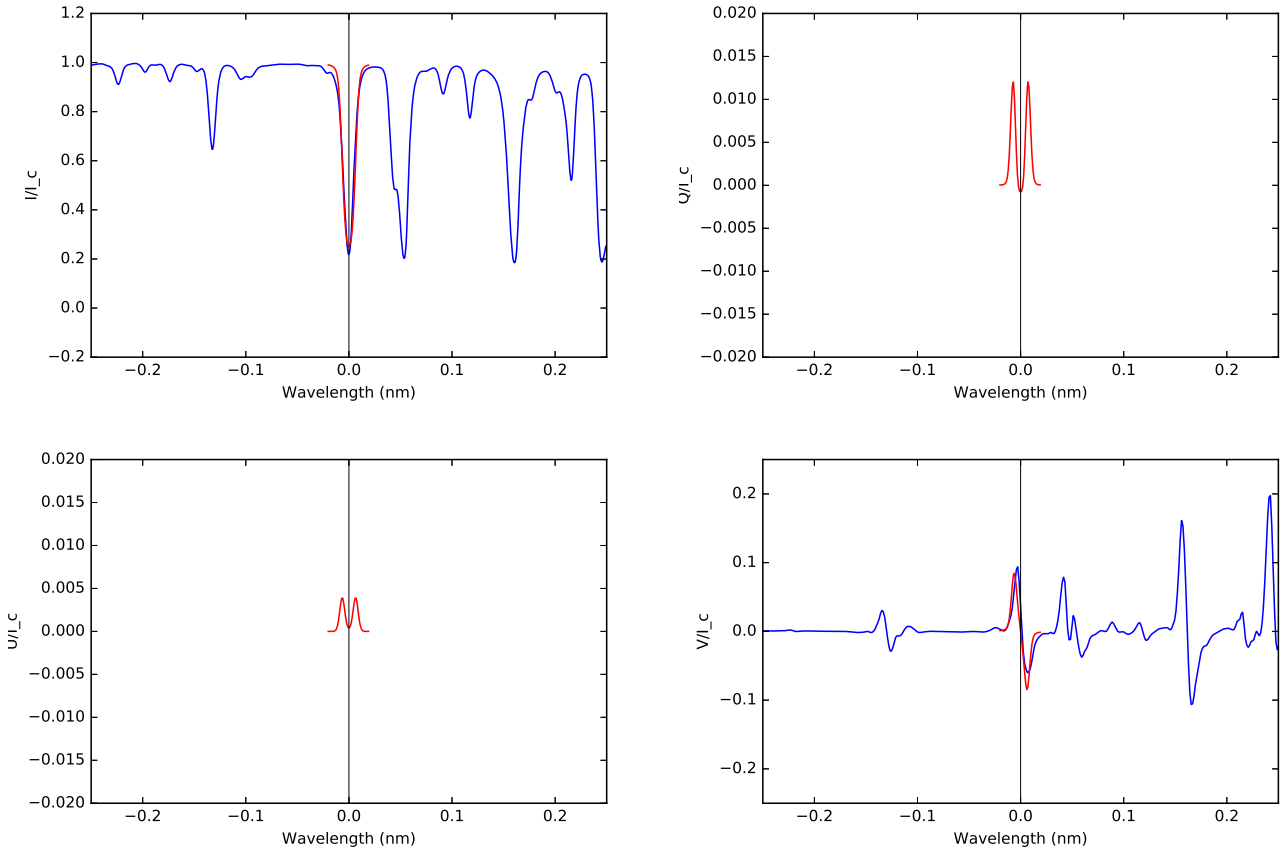

Figure 4: Synthetic Stokes profiles of Stokes I (top left), Q (top right), U (bottom left) and V (bottom right) for the Ca I line at 526.171 nm in the synthesis with 1500 G.

V amplitudes for all lines from the 1500 G synthesis (see Tables 4 and 5). I identified a subset of six lines with or without linear polarization (cf. Table 1) for testing the approach of inferring polarimetric telescope properties. These lines were selected because of their large line depths and polarization amplitudes, the absence of line blends (cf. Figs. 2–4, Figs. 18–19), and a continuous wavelength coverage from 400–615 nm. Figures 2 to 4 show the synthetic profiles of the lines at 459, 526 and 615 nm analyzed in this study. Neutral lines, such as Ca I at 526.2 nm, are generally better suited than singly-ionized lines because the latter disappear in a cool atmosphere such as present in sunspots and pores. The Ca I line at 526 nm has small LP (ratio of V/LP ≈ 10) while the lines at 459 and 615 nm have zero LP. The only line that has been previously used for calibration purposes is Fe II at 614.9 nm (Lites 1993; Cabrera Solana et al. 2005; Elmore et al. 2010).

Table 1: Transition parameters, line depth and maximal polarization amplitudes at 1500 G.

Element	Ion. State	λ_0 [nm]	Exc. Pot. (eV)	log (gf)	Transition	$g_{\rm eff}$	LP?	Line Depth [%]	Max. $\lvert Q/I\rvert$	Max. $\lvert U/I\rvert$	Max. $\lvert V/I\rvert$
Mn	I	425.766	2.953	-0.70	4D 0.5- 4P 0.5	1.333	no	81.0	0	0	0.216
Ti	II	431.490	1.1609	-1.104	4P 0.5- 4D 0.5	1.333	no	92.1	0	0	0.156
Cr	II	458.820	4.071	-0.64	4D 0.5- 6F 0.5	0.333	no	81.2	0	0	0.074
Fe	I	514.174	2.424	-2.238	3P 1.0- 3D 1.0	1.000	low	84.3	0.003	0.011	0.138
Ca	I	526.171	2.521	-0.73	3D 1.0- 3P 1.0	1.000	low	79.7	0.003	0.008	0.127
Fe	II	614.923	3.889	-2.8	4D 0.5- 4P 0.5	1.333	no	45.6	0	0	0.134

4 Application of Lines without LP for Polarimetric Calibration

The following expression is valid for the Stokes vector $\vec{S}$ after propagation through the telescope optics for a spectral line without LP where $\mathbf{T}$ is the Mueller matrix of the telescope and $(I', 0, 0, V')^T$ is the light incident on the telescope:

$$\vec{S} = \begin{pmatrix} I \\ Q \\ U \\ V \end{pmatrix} = \begin{pmatrix} T_{11} & T_{12} & T_{13} & T_{14} \\ T_{21} & T_{22} & T_{23} & T_{24} \\ T_{31} & T_{32} & T_{33} & T_{34} \\ T_{41} & T_{42} & T_{43} & T_{44} \end{pmatrix} \begin{pmatrix} I' \\ 0 \\ 0 \\ V' \end{pmatrix} \tag{1}$$

The observed linear and circular polarization are then given by:

$$Q = T_{21} \cdot I' + T_{24} \cdot V' \tag{2}$$
$$U = T_{31} \cdot I' + T_{34} \cdot V' \tag{3}$$
$$V = T_{41} \cdot I' + T_{44} \cdot V' \, . \tag{4}$$

The cross-talk $I \rightarrow QUV \equiv T_{i1} \cdot I$ can easily be measured at continuum wavelengths outside of any spectral line and subsequently be compensated for, which yields:

$$Q_{corr} = T_{24} \cdot V' \tag{5}$$
$$U_{corr} = T_{34} \cdot V' \tag{6}$$
$$V_{corr} = T_{44} \cdot V' \, . \tag{7}$$

With that, the ratios Q_{corr}/V_{corr} and U_{corr}/V_{corr} correspond to the ratios of telescope matrix entries T_{24}/T_{44} and T_{34}/T_{44}. With a determination of Q_{corr}/V_{corr} and U_{corr}/V_{corr} from observational data taken at a given telescope, one can thus obtain the ratio of telescope matrix entries at different times

and telescope geometries. If a model of the polarimetric properties of the corresponding telescope is available, one can then infer the set of model parameters that best reproduce the observed Q_{corr}/V_{corr} and U_{corr}/V_{corr} ratios. The approach can also be used in the opposite direction for test purposes such that if a telescope correction is applied using a set of parameters and there is some residual LP, it can be deduced that the model parameters are incorrect and need to be updated. For lines with small linear polarization, Eqs. (5)–(7) are not strictly valid, but with $V/\mathrm{LP} \approx 10$ the contribution from T_{22}, T_{23}, T_{32} and T_{33} is still very small.

5 Observations

To test the usage of spectral lines without linear polarization for the inference of telescope parameters, V. Pillet, C. Beck, and myself ran an observing campaign at the Dunn Solar Telescope (DST) in Sunspot, NM on March 8–31, 2016. We combined the Spectropolarimeter for Infrared and Optical Regions (SPINOR; Socas-Navarro et al. 2006), the Facility Infrared Spectropolarimeter (FIRS; Jaeggli et al. 2010) and the Interferometric Bidimensional Spectrometer (IBIS; Cavallini 2006; Reardon & Cavallini 2008) in order to obtain spectropolarimetric data in different wavelength regions at the same time. A dichroic beam splitter (BS) was used to separate infrared (IR) and visible (VIS) wavelengths. FIRS was fed with the IR light while the VIS light was split evenly between IBIS and SPINOR by an achromatic 50-50 BS. IBIS and FIRS observed spectral lines with a regular Zeeman pattern (617.3 nm, 630.25 nm, 656 nm, 854 nm, 1083 nm and 1565 nm) which were not used for the current study. Both IBIS and FIRS were subsequently dropped from the setup on March 17 and 18, respectively, and the corresponding BSs in the light feed were removed or replaced with flat mirrors to increase the light level in SPINOR.

SPINOR was set to observe the six lines with small or without LP listed in Table 1 in two different configurations. In the first configuration (setup 1), the lines at 426 nm, 431 nm, and 615 nm were observed from March 8-17, while the lines at 459 nm, 514 nm, 526 nm were covered from March 17-24 (setup 2). The wavelength range always covered additional lines with a regular Zeeman pattern as well (Figs. 5–7, Figs. 20–22). The spectral sampling was done between 3–5 pm. The exposure time was between 22–125 ms and the integration time was between 10–30 s depending on the setup of SPINOR and the light feed. The spatial sampling in the scanning direction was $0\farcs75$ ($0\farcs37$) in setup 1 (setup 2) and the sampling along the slit was about $0\farcs35$ in all cases. The slit width was 100μm corresponding to about $0\farcs75$ on the Sun.

In each configuration, several maps of the sunspots in NOAA 12519 and 12524 with $30'' \times \approx 100''$ extent were acquired each day. We also took a few observations of small pores and quiet Sun at disc center to sample regions with smaller polarization amplitudes for comparison. In total, about 30 data sets were obtained in each setup.

Given the amplitude of the interference fringes at all wavelengths shorter than 450 nm (Figs. 20 and 21) and the fact that 514 nm and 526 nm are close to each other, we only analyzed the data at 459 nm, 526 nm and 615 nm.

6 Data Analysis

6.1 Preparation of Input Data

This section addresses the methods I used to infer the parameters of the DST telescope model from the observations and the steps required to prepare input data corresponding to Equations (5)–(7) for all locations with significant polarization signal.

6.1.1 Reduction of SPINOR Data

I first reduced the data without applying the correction for the telescope polarization, but with a correction for $I \rightarrow QUV$ cross-talk, using the standard SPINOR data pipeline[10]. The $I \rightarrow QUV$ cross-talk was determined in a continuum wavelength range close to the line of interest without linear polarization. The values of the $I \rightarrow QUV$ cross-talk were stored for later use because they contain the information on the first column of the telescope matrix. After this step, a two-dimensional (2D) Fourier filtering in Stokes QUV was applied in order to reduce the amplitude of interference fringes. The Fourier filter was set to remove spectral frequencies within a manually set frequency range that were constant along the slit, i.e., only fringes with a spatial frequency of zero were removed. The fringe pattern in all of the data also contained higher-order fringes that were not taken out. Since the polarization signal can easily extend along 50 % of the slit length in observations of active regions, any attempt to include higher spatial frequencies can remove genuine polarization signal as well. The fringe amplitude, period and phase were also not constant across the spectrum in both the spatial and spectral domain, thus only the primary fringe component could be corrected for. The example slit spectra in Figures 5–7 show spectra after the correction for the strongest fringe pattern.

6.1.2 Determination of Locations with Significant Polarization Signal

To determine the locations inside the field of view (FOV) that showed significant polarization signal, the maximal polarization degree, $p_{\max}$, of every profile was calculated by

$$p_{\max} = \max[p(\lambda)]_{|\Delta\lambda} = \max[\sqrt{Q^2 + U^2 + V^2}/I(\lambda)]_{|\Delta\lambda} \tag{8}$$

in a small wavelength range $\Delta\lambda$ around a spectral line with strong polarization signal. The line need not have been the one with low or zero LP as each spectral range also covered stronger lines (Figures 5–7).

From the analysis of all profiles, spatial maps of the polarization degree in 459 nm, 526 nm, and 614 nm were created for all observations (see Figure 8). These maps were used to determine the locations of significant polarization signal through a threshold value of 0.01–0.03 by rejecting all profiles with lower polarization amplitudes. In addition, by requiring that the profiles above the threshold belong to a spatially connected area with some minimal size, I masked out everything but sunspots and pores. For the 459 nm data, in several cases, the fringe pattern in the polarization signal was too strong to use the maps of $p_{\max}$. Instead, a threshold in the map of the continuum intensity was used to separate the umbra and penumbra of the sunspot from the brighter quiet Sun and to only retain the profiles located inside the sunspot.

6.1.3 Determination of $V \rightarrow QU$ Cross-Talk

A determination of the $V \rightarrow QU$ cross-talk from the ratio of observed profiles Q/V and U/V can become unreliable for small values of V in the presence of noise. Therefore, a linear fit of $QU_{obs}(\lambda) = \alpha_{QU} V_{obs}$ was made for all profiles above the polarization threshold (see, e.g., Figure 9). Only the close surroundings of the spectral line of interest without LP were used to avoid contamination with line blends.

To verify the quality of the fit, the obtained cross-talk values α_{QU} were used to correct the observed Q and U spectra by $QU' = QU - \alpha_{QU} \cdot V$ (top row of Fig. 9). The correction can be applied to the full spectral range. In the example of Fig. 9, the change between Stokes U and U' is

[10] http://nsosp.nso.edu/dst-pipelines

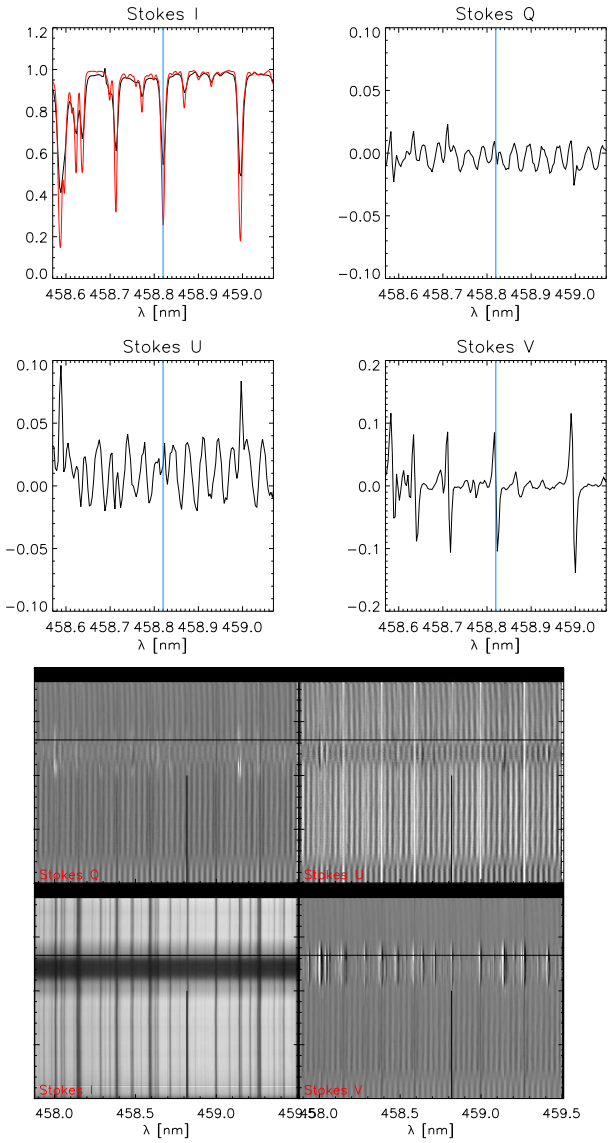

Figure 5: Example spectra at 458.8 nm. Top panels: individual $IQUV$ profiles from the location indicated with a horizontal black line in the lower panels. The red lines show the corresponding profiles from the FTS atlas. Bottom panels: slit spectra of (clockwise, starting left bottom) $IQUV$ on a cut across the center of a sunspot. The line without LP is indicated by a black vertical bar.

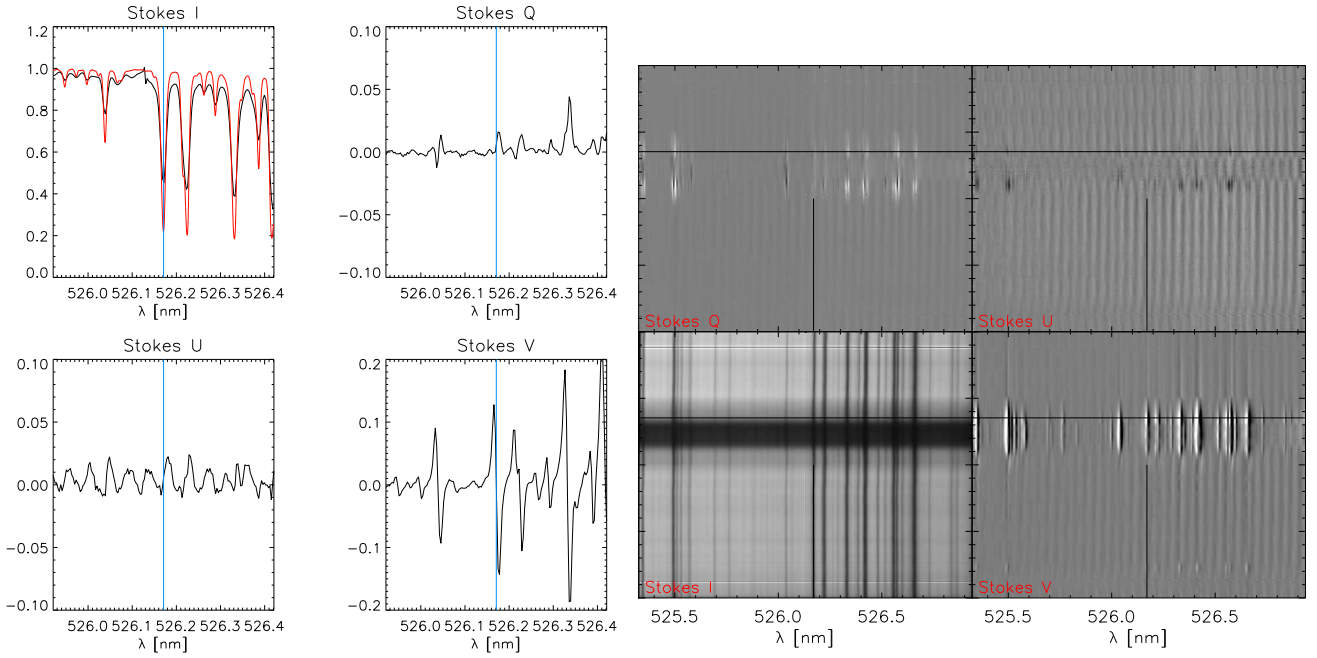

Figure 6: Same as Fig. 5 for 526.2 nm.

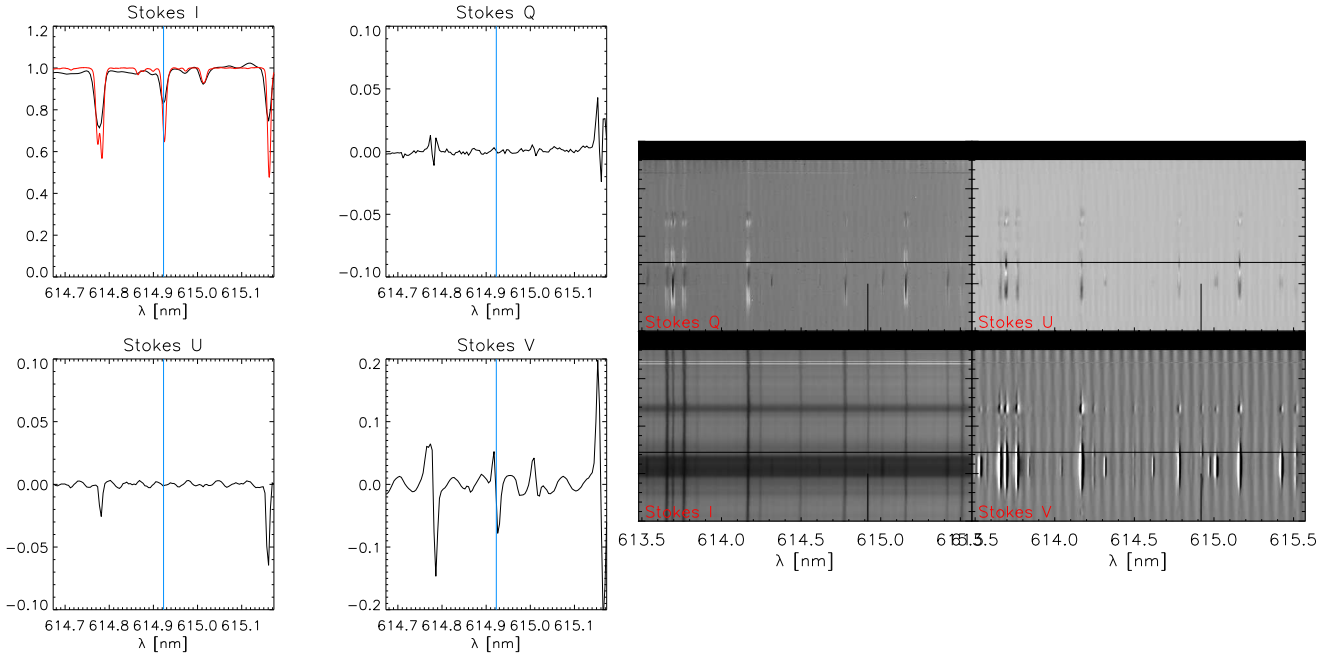

Figure 7: Same as Fig. 5 for 614.9 nm.

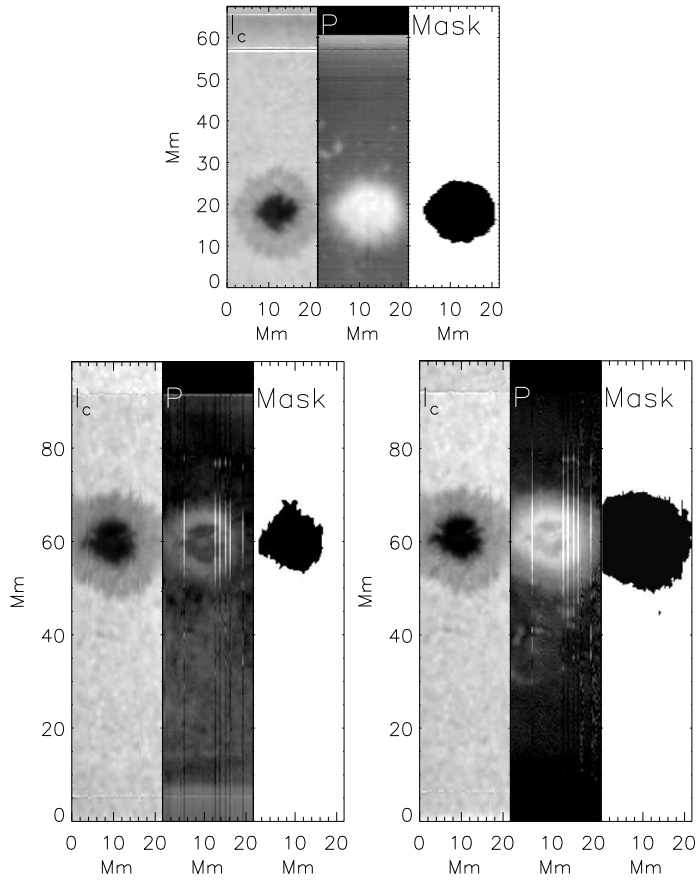

Figure 8: Maps of one scan at 459 nm (bottom left panel), 526 nm (bottom right panel), and 614 nm (top panel). Left to right: continuum intensity, I_c, polarization degree $p_{\max}$, and mask of significant polarization signal. The vertical bright stripes in $p_{\max}$ for 459 nm and 526 nm were caused by a temporary loss of the synchronization between polarization modulation and exposures during the scanning.

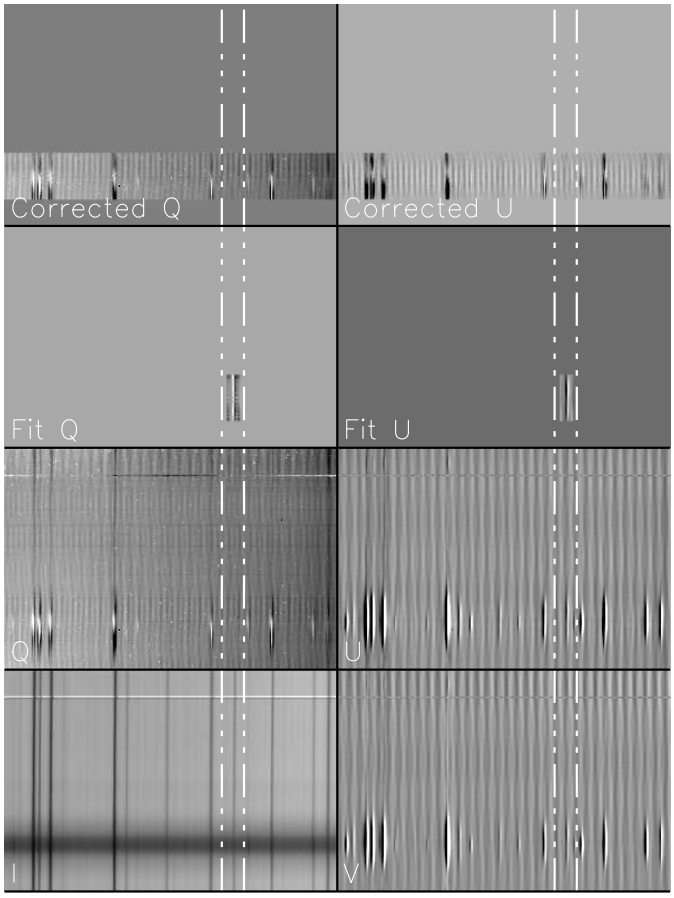

Figure 9: Example slit spectrum at 614 nm with the fit of $V \rightarrow QU$. Left column, bottom to top: Stokes I, Stokes Q, the fitted $Q = \alpha_Q \cdot V$ and the Stokes Q signal after correction, $Q' = Q - \alpha_Q \cdot V$. Right column, bottom to top: Stokes V, Stokes U, the fitted $U = \alpha_U \cdot V$ and the Stokes U signal after correction, $U' = U - \alpha_U \cdot V$. The vertical dash-dotted lines indicate the location of the 614.9 nm line.

obvious, where the latter has no residual LP in the 614.9 nm line, while all other Zeeman-sensitive lines in the wavelength range have changed from a Stokes V-like shape (a negative lobe and a positive lobe corresponding to black and white coloring) to regular LP signals by the correction. The fit thus correctly retrieves the $V \rightarrow QU$ cross-talk values.

The values of α_{QU} obtained from the individual profiles were averaged along the slit over all profiles in the mask to retrieve $< \alpha_{QU} > (t)$ because all profiles along the slit were taken at the same time. The time, t, is used as a placeholder for the telescope geometry that contains the telescope pointing in elevation and azimuth and the position of the coudé table. The numbers used in the calculation of the DST telescope model are actually azimuth(t), elevation(t), and table angle(t). Figure 10 shows the values of $< \alpha_{QU} > (t)$ at 614.9 nm for one of the observations. For comparison, the values of the corresponding telescope matrix entries predicted by the "standard" DST telescope model, i.e., using the telescope parameters determined in 2010, are overplotted in red. The modulus of the values agrees to first order, but the agreement is not very close (cf. Sect. 6.2.2 below).

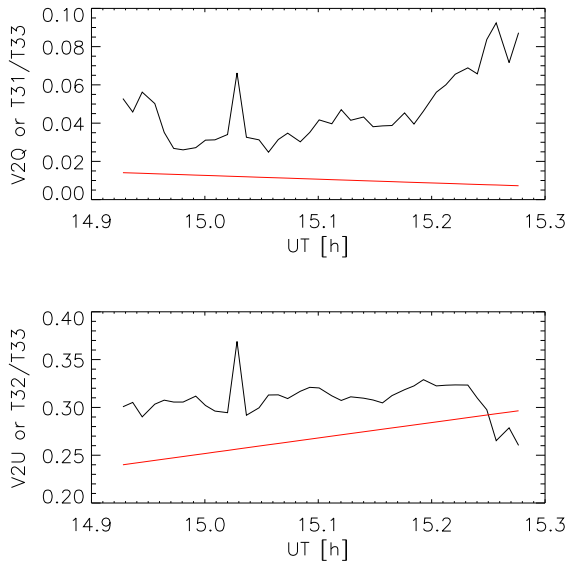

Figure 10: Cross-talk from $V \rightarrow QU$ averaged along the slit for the map at 614.9 nm shown in Fig. 8 (black lines). The red lines show the values of the DST telescope model for $\frac{T_{31}}{T_{33}}$ and $\frac{T_{32}}{T_{33}}$, respectively, using the parameters determined in 2010.

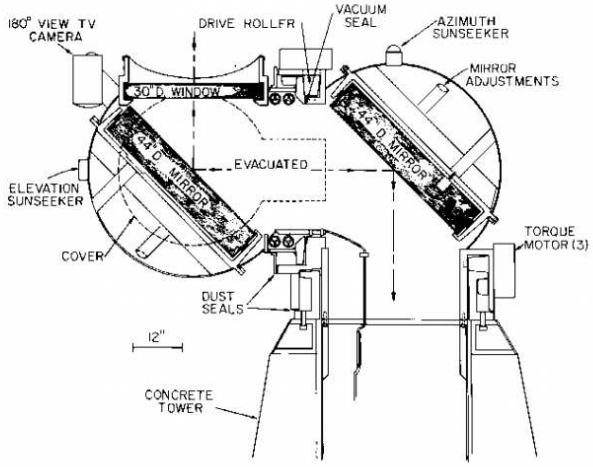

Figure 11: Top turret mirrors of the DST telescope.

6.2 Fit of DST Telescope Model

6.2.1 DST telescope model

The polarization model of the DST has been described in detail in Skumanich et al. (1997) and Socas-Navarro et al. (2011). The optical train consists of the entrance window to the evacuated steel tube, the two flat turret mirrors at an angle of incidence (AOI) of 45 degrees in an alt-azimuth

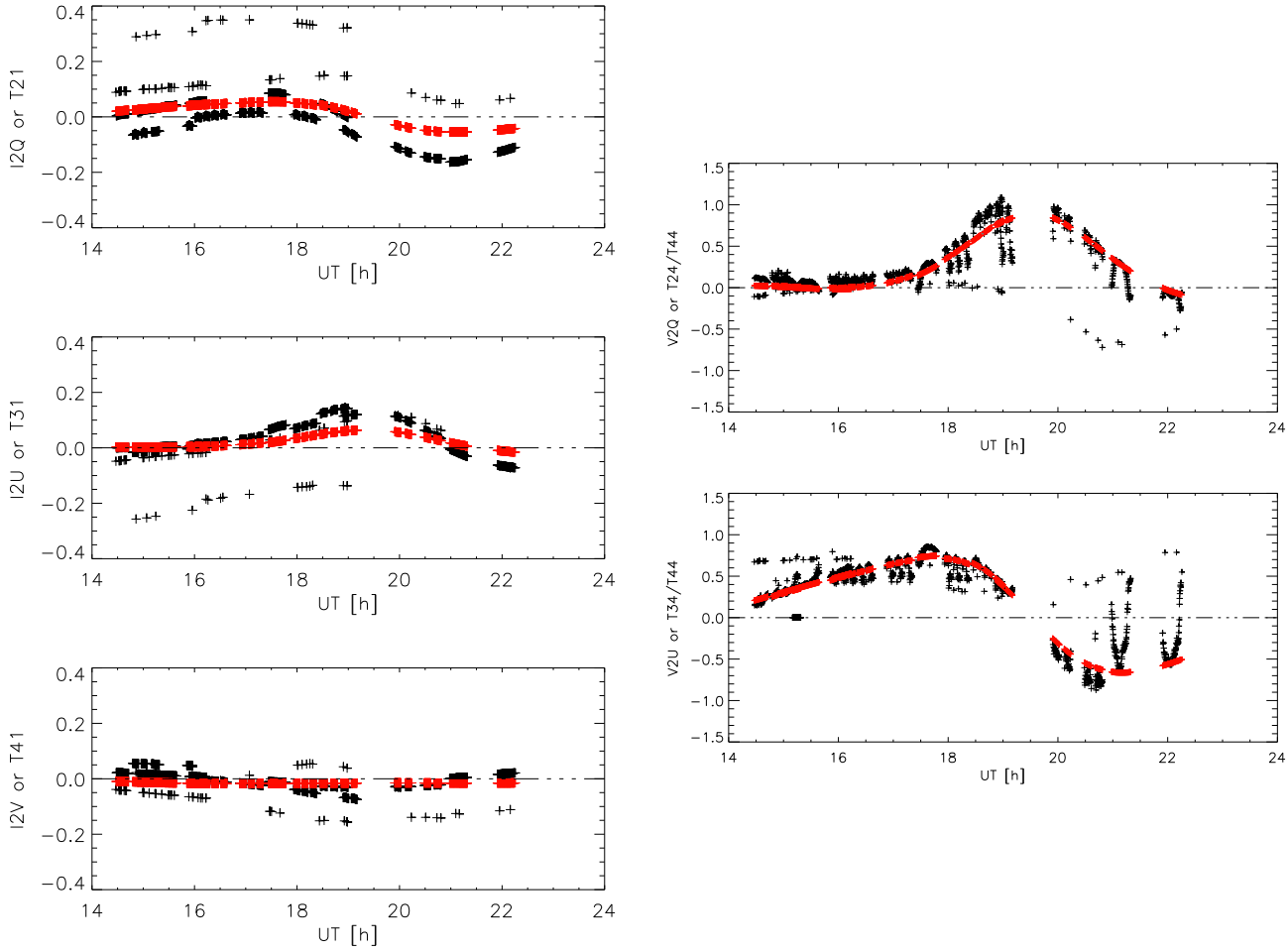

Figure 12: Input to the fit of telescope parameters derived from all observations of 526.2 nm during the campaign. Left column, top to bottom: observed $I \rightarrow QUV$ cross-talk (black crosses). Right column, top to bottom: $V \rightarrow QU$ cross-talk. The red crosses show the corresponding values of the DST telescope model using the 2010 model parameters.

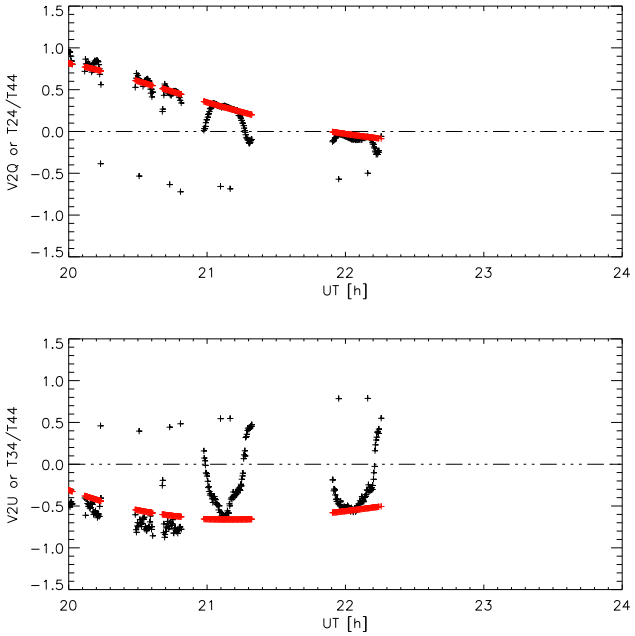

Figure 13: Magnification of the $V \rightarrow QU$ cross-talk at 526.2 nm for observations taken between UT 20:00 - 22:00. Individual maps lasted about 30 min. Most scans show a dominant parabolic shape of the cross-talk values (seen also in Fig. 12). Only the central position of the scan yields a value that agrees with the 2010 telescope model.

mounting, the primary mirror at an AOI of less than 1 degree and the exit window of the vacuum tube (see Fig. 11). Both turret mirrors are described with the same set of parameters, the ratio of reflectivities parallel and perpendicular to the plane of reflection, $X = r_s/r_p$, and the retardance τ_{mirror}. The primary mirror is modeled as an ideal mirror because of the small AOI. Entrance (EN) and exit (EX) windows are modeled independently as ideal retarders with two parameters each, the retardance $\tau_{\mathrm{EN,EX}}$ and the orientation of the fast axis $\beta_{\mathrm{EN,EX}}$. To capture the orientation of the telescope model relative to the instrument calibration unit that is located on the rotating coudé table, an offset angle θ_{offset} between the telescope model and coudé table is used as a free parameter. The known geometry of the telescope at any given moment in time is expressed by the elevation, azimuth and the relative orientation of the coudé table (table angle).

The free parameters of the DST telescope model are usually determined from measurements with a telescope calibration unit (TCU). The TCU consists of an array of sheet polarizers that is placed on top of the entrance window. The TCU is motorized and can be rotated in a full circle. The evaluation of the data and the results are described in detail in Socas-Navarro et al. (2011). In the current study, I used the parameter set that was determined using the TCU in 2010 as a reference.

6.2.2 Input Data for Fit of Telescope Model

The input data for the fit of the telescope model parameters have two components (see Fig 12); the values of the $I \rightarrow QUV$ cross-talk that correspond to the first column of the telescope matrix, and the values of the $V \rightarrow QU$ cross-talk that correspond to the ratios of the matrix entries T_{24}/T_{44} and T_{34}/T_{44}. Both quantities were determined in individual profiles and then averaged along the slit

because each slit spectrum corresponds to one moment in time. The geometrical input parameters (elevation, azimuth, table angle) were extracted from the file headers of each spectrum. In the following figures, I plot all the values just as a function of time for simplicity. The data of each wavelength range were taken within about a week, so the solar position was similar at the same time on different days. All calculations, however, always used the actual telescope geometry at the moment of the observations.

After plotting the corresponding curves for the data at any of the three wavelengths, I noticed a parabolic pattern in the $V \rightarrow QU$ cross-talk data which did not match the 2010 telescope model, but rather touched its predicted values only at one scan step (Fig. 12). The parabolic shape is very obvious for some of the individual maps (Fig. 13). It presumably was caused by the specific setup for the observations. The SPINOR modulator had been removed from its location in the collimated beam upstream of all instruments and had been placed as close to the slit as possible to prevent interference with the polarization measurements with FIRS and IBIS, and to minimize the image motion caused by a wedge in the modulator optics. The spatial scanning of SPINOR is achieved by moving part of the spectrograph, i.e., the slit unit, the first fold mirror and the collimator, laterally. The spatial scanning therefore moved the slit relative to the modulator, sampling different areas on the modulator depending on the scan position. The polarimetric calibration of the instrument, however, was only done with the slit centered. Together, this led to a variation of the polarization modulation across the FOV that was not removed by the calibration process. Thus, all of the data points apart from the central slit position of each map were dropped.

6.2.3 Fit of Telescope Model Parameters

I then attempted to fit the open parameters of the DST telescope model, X and τ for the turret mirrors, the retardance $\tau_{\mathrm{EN,EX}}$, and the orientation of the fast axis $\beta_{\mathrm{EN,EX}}$ of the entrance and exit windows to the observed $I \rightarrow QUV$ and $V \rightarrow QU$ cross-talk values considering only the central step of each observation.

It was immediately obvious that there is a sign conflict between the observations and the model in the $I \rightarrow QUV$ cross-talk (orange and red or blue pluses in Fig. 14) that were opposite of each other. A mismatch of signs between the 2010 model values and the more recent SPINOR data pipeline was already known. For the application of the telescope correction using the 2010 values, the offset angle θ_{off} of about 90 degrees in 2010 had to be changed to $\theta_{off} + 90 \sim 180$ degrees. There are unfortunately multiple reasons that could cause this sign conflict. A difference in the selection of beams when merging the Stokes vectors would flip the signs of Stokes Q, U and V. The linear polarizer of the calibration unit (CU) was taken out and installed back into the CU a few times between 2010 and 2016. If the optical axis got switched by 90 degrees when replacing the polarizer, that also would flip the signs in some of the Stokes parameters. V. Pillet, C. Beck, and myself were not able to identify the source for the sign mismatch. We therefore used an ad-hoc correction by flipping the sign of the observed $I \rightarrow QUV$ cross-talk values and used an offset angle of 180 degrees as initial value. The $V \rightarrow QU$ values are not affected because they represent a ratio of Stokes parameters.

A second point that became obvious instantly was that the retardances of the windows were not constrained by the data. When trying to fit the retardances of the windows and of the turret mirrors at the same time, the former were running off to unreasonably large values of more than 20 degrees in retardance. Depending on the initial values of the fit, the retardances of the two windows were sometimes changing in opposite directions with sort of a zero net retardance (see also Socas-Navarro et al. 2011, their Sect. 3).

Therefore the fit was modified to a two-step procedure. In the first step, only X, τ and θ_{off}

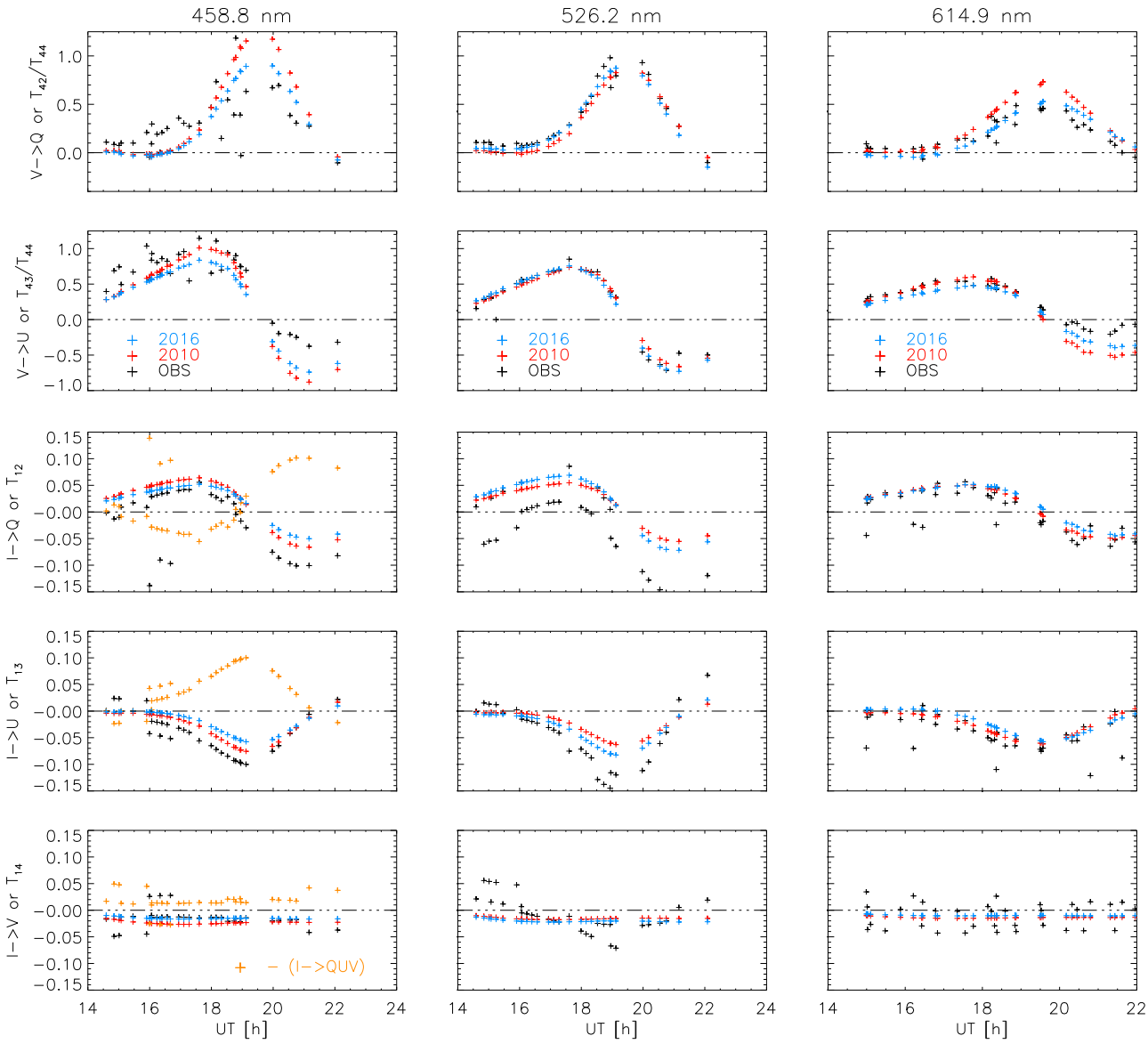

Figure 14: Fit of telescope parameters at 458.8 nm, 526.2 nm, and 614.9 nm. Top to bottom: observed cross-talk of $V \to Q$ (black crosses), $V \to U$, $I \to Q$, $I \to U$, and $I \to V$. The blue (red) crosses show the corresponding values of the DST model using the 2016 (2010) model parameters. The orange pluses in the lower three panels of the leftmost column show the original $I \to QUV$ values before flipping their sign.

Table 2: Literature values, best-fit results and error estimates of telescope parameters.

	X	τ [deg]	θ_{off} [deg]	$\tau_{\rm EN}$ [deg]	$\beta_{\rm EN}$ [deg]
	458.8 nm				
Literature	1.057	165.8	–	–	–
2010 TCU	1.101	148.9	93.1	3.0	138.6
2016 fit	1.077	153.2	178.2	0.6	22.0
σ	± 0.033	± 0.5	± 0.7	± 0.6	–
	526.2 nm				
Literature	1.059	167.7	–	–	–
2010 TCU	1.083	155.0	93.1	2.3	138.6
2016 fit	1.108	154.3	182.0	0.6	22.0
σ	± 0.035	± 0.5	± 0.7	± 0.6	–
	614.9 nm				
Literature	1.065	169.5	–	–	–
2010 TCU	1.080	157.8	93.1	2.1	138.6
2016 fit	1.074	162.7	174.2	0.4	22.0
σ	± 0.036	± 0.6	± 1.1	± 0.8	–

were allowed to vary, while in the second step the retardance, position angle of the entrance window and θ_{off} were varied. The exit window was not considered due to its small size and set to a unity matrix. The retardance of the mirrors was found to be already able to reproduce the observations very well, so that the window's retardance in the second step stayed close to zero. Note that in the DST telescope model, the window retardance to some extent only gets added to that of the mirrors, with the orientation of its optical axis as one more degree of freedom. The final fit procedure in our case then only used X, τ, θ_{off}, $\beta_{\rm EN}$ and $\tau_{\rm EN}$.

7 Results

7.1 Fit Quality

Figure 14 shows the final result of the fit (blue pluses) together with the corresponding curves when using the 2010 model parameters (red pluses) and the observations (black pluses) for all three wavelengths. The input data (observations) at 458.8 nm shows the largest scatter that presumably resulted from the residual fringe pattern (Fig. 5). The differences between the new determination (the fit) and the 2010 values are rather small, only a few percent, however both parameter sets provide a good fit to the input data. The match of the observations and the telescope model with any parameter set is slightly worse in the afternoon for times later than about UT 19:00.

7.2 Ratio of Reflectivities $X = r_s/r_p$

Table 2 lists the results for all free fit parameters from the current determination and the 2010 measurements. In addition, I calculated the values of X and τ for the turret mirrors assuming optically thick coatings (i.e. light does not penetrate the aluminum coating of the mirror and there is no influence of the underlying glass substrate) using the literature values at each wavelength given in the Handbook of Chemistry and Physics. For the ratio of reflectivities X, there is no clear wavelength trend in either the 2010 or 2016 results, while the literature values show a monotonic

decrease with increasing wavelength (see Fig. 15). All values for X determined from measurements at the DST are around 1.09±0.1, while the literature values are about 0.02-0.05 lower (see also Socas-Navarro et al. 2011, their Fig. 8). The value of X is only weakly constrained by the $V \rightarrow QU$ cross talk, where it cancels out for a single mirror,

$$V \rightarrow Q \equiv T_{24}/T_{44} = \frac{-2\,X\,\sin\,\tau}{2\,X\,\cos\,\tau} = \tan\,\tau \neq \mathrm{f}(X)\,. \tag{9}$$

The sensitivity test described in Sect. 7.4 below confirms this. Within the assumed error range, the measurements of X from data acquired at the DST agree well.

7.3 Window and Mirror Retardance τ

The mirror retardance alone was found to already cover the needed value and to provide a good fit. The second step of the two-step fit using the entrance window retardance as described in Sect. 6.2.3 above yielded a window retardance τ_{EN} of less than 1 degree, therefore making the window seem negligible. Note that the initial value of the orientation of the optical axis of the window for the fit was 22 degrees. This was not significantly changed in the fit (last column of Table 2), which would support the assumption that the window does not contribute to the polarization properties of the optical train, or its contribution cannot be separated from that of the mirrors given the input data.

The retardance of the turret mirrors τ increases monotonically with wavelength in all cases, i.e., for the 2010 fit, the 2016 fit, and the literature values (see Fig. 15). The 2010 and 2016 fit have rather similar values, while the literature values are offset from them by about 5 degrees. The literature values do not take any information obtained at the DST into account, so their global offset from both fit values is uncritical, whereas the fit values themselves agree well.

Figure 15 shows a plot of both X and τ for the turret mirrors for all available values for completeness. The error bars were taken from the estimates in the next section.

7.4 Sensitivity Test and Error Estimate

To check the sensitivity of the fit and the telescope model to changes in the model parameters, I varied X and τ of the turret mirrors by -0.1 to 0.1 and -10 to 10 respectively around the best-fit value, while keeping the window properties at the best-fit values. Figure 16 shows the reaction of the telescope model in the $I \rightarrow QUV$ and $V \rightarrow QU$ cross-talk values to these changes at a wavelength of 614.9 nm. The other two wavelengths at 459 nm and 526 nm showed a similar behavior.

The $V \rightarrow QU$ cross-talk reacts only weakly to changes in X. Only for values of X that were far outside the range of variation used here, e.g., $X < 0.5$ or $X > 2$, a significant change was seen. This is due to the fact that the DST contains two mirrors that rotate relative to each other when tracking the Sun, while X cancels out for a single mirror as shown by Eq. (9) above. The $I \rightarrow QUV$ cross talk on the other hand reacts strongly to changes in X, while it is completely unaffected by changes in τ.

I used the sensitivity test to estimate a reliability interval of $\pm 3\sigma$ for the fit procedure by determining the variation of X or τ that led to a change of the $I \rightarrow QUV$ or $V \rightarrow QU$ cross talk by 0.01 on average. The scatter in the observational values, e.g., for $I \rightarrow V$, is of about that order of magnitude, so a variation by 1 % can be taken as the reliability level of the input data. This yielded a range of about ±0.035 for X, $\pm(0.5 - 0.8)$ degrees for the retardances τ of the turret mirrors and the entrance window, and ±1 degree for the offset angle (see Table 2). At the very small retardance best-fit value of the entrance window of less than a degree, the orientation of the window retardance was nearly unconstrained. All three spectral ranges gave very similar results.

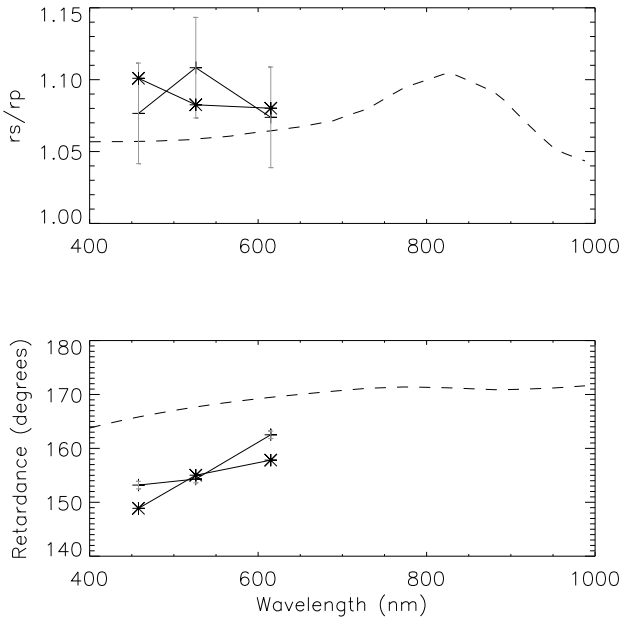

Figure 15: Values of X (top panel) and τ (bottom panel) for the literature values (dashed lines), the 2010 telescope model parameters (asterisks), and the current 2016 fit results (crosses). The vertical grey lines show error estimates of $\pm$ 0.035 (top panel) and $\pm$ 1 degree (bottom panel).

Table 3: Residual rms $V \rightarrow QU$ cross talk.

	$V \rightarrow Q$	$V \rightarrow U$
	458.8 nm	
Uncorrected	0.27	0.43
2010 TCU	0.11	0.12
2016 fit	0.10	0.12
	526.2 nm	
Uncorrected	0.33	0.47
2010 TCU	0.04	0.06
2016 fit	0.03	0.05
	614.9 nm	
Uncorrected	0.17	0.25
2010 TCU	0.08	0.11
2016 fit	0.09	0.11

7.5 Residual cross talk with telescope correction

To test the fit quality, I applied the telescope correction to the observations using the parameter sets from 2010 and 2016 prior to running the determination of the $I \rightarrow QUV$ and $V \rightarrow QU$ crosstalk in the same way as before. With the telescope correction, all cross-talk values should be close to zero. Figure 17 shows that this is indeed the case for the $V \rightarrow QU$ cross talk. The rms fluctuations of the $V \rightarrow QU$ cross talk are given in Table 3 for all wavelengths. With the application of the telescope correction, they reduce from the uncorrected case with about 20–30 % rms to 3–10 %

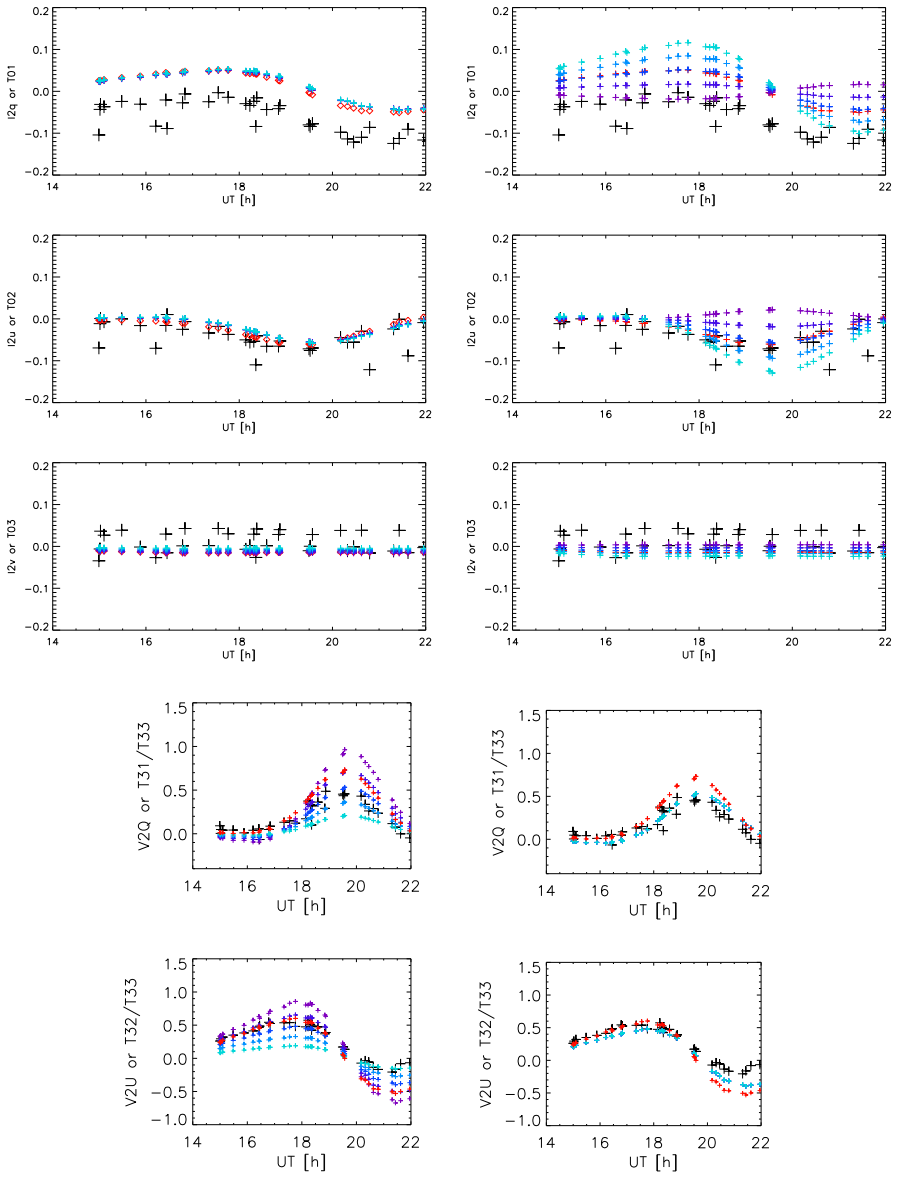

Figure 16: Sensitivity test of the telescope model at a wavelength of 614.9 nm. Top three rows: change in $I \rightarrow QUV$ for a variation of the mirror retardance τ (left column) and the ratio of reflectivities X (right column). Observations are given by black pluses, while the red pluses correspond to the 2010 parameter set. τ and X were varied from -10 to 10 and -0.1 to 0.1, respectively. The resulting curves are indicated by the series of blue to purple pluses. Bottom two rows: change in $V \rightarrow QU$ for a variation of the mirror retardance τ (left column) and the ratio of reflectivities X (right column).

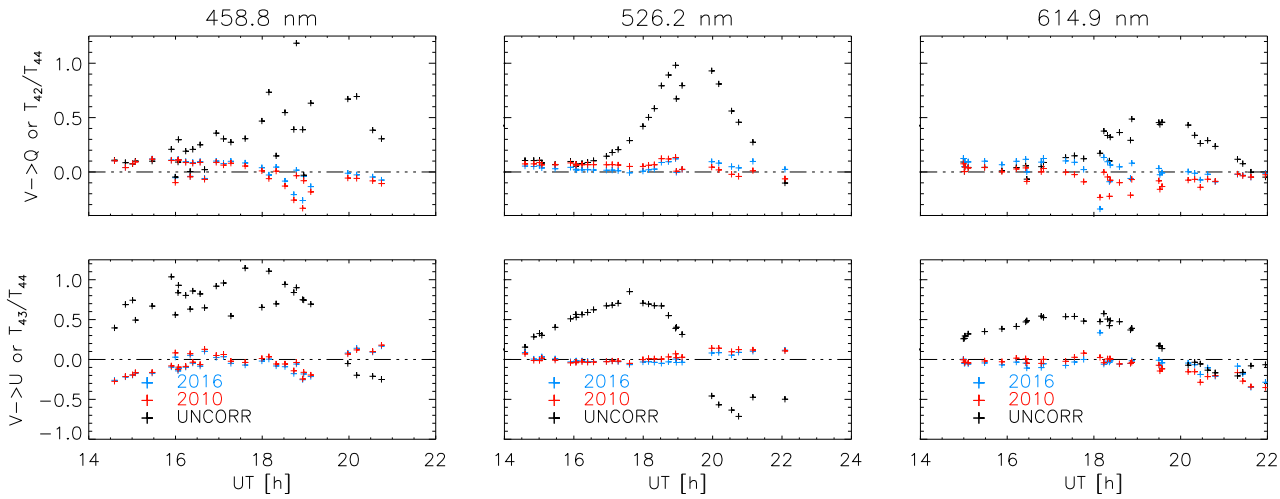

Figure 17: Residual $V \rightarrow Q$ (top row) and $V \rightarrow U$ (bottom row) cross talk after applying the telescope correction. Left to right: at 458.8 nm, 526.2 nm and 614.9 nm. Black pluses: observations without telescope correction. Red/blue pluses: observations with a telescope correction using the 2010/2016 model parameters.

rms after the correction. The new determination in 2016 yields a slightly lower rms than the 2010 parameter set, but usually only by about 1 %.

The residual cross-talk level thus stays at a value of (3-10)$\times 10^{-2}$ regardless of which correction is applied. The error when applied to correct solar observations is then about one order of magnitude lower, given that the maximal polarization amplitudes in, e.g., the solar photosphere, are limited to about 0.3 in the very umbra of sunspots by the thermal broadening.

8 Summary & Discussion

I acquired a series of spectropolarimetric observations of active regions containing sunspots over a few days in six different spectral lines with or without negligible linear polarization signals (cf. Table 1). From the analysis of the cross-talk between intensity and polarization, $I \rightarrow QUV$, and the cross-talk between circular and linear polarization, $V \rightarrow Q$ and $V \rightarrow U$, I was able to infer the parameters that characterize the model of the polarization properties of the DST for a subset of three spectral lines, and hence three wavelength regions at 459, 526 and 615 nm (cf. Table 2).

8.1 Method

Unlike most other calibration techniques in use for current ground-based solar telescopes (Skumanich et al. 1997; Beck et al. 2005; Selbing 2010; Socas-Navarro et al. 2011), this approach does not require any additional optics other than a spectropolarimeter with medium to high spectral resolution. The method does not rely on any assumptions for lines without intrinsic linear polarization, while for the other lines the linear polarization is assumed to be negligibly small (Lites 1993; Sanchez Almeida & Vela Villahoz 1993; Vela Villahoz et al. 1994).

The analysis procedure is automatic to a high degree. After identification of the corresponding spectral line to be used, the thresholds in polarization degree or continuum intensity for the selection

of spatial positions to be included, and the initial values for the least-squares fit are the only items which must be manually provided.

The method is based on a statistical approach. The data to be analyzed does not have to be acquired consecutively over a few days as done in our case, but can be collected over a longer period as long as the telescope properties did not vary significantly within that time frame. In addition, the spatial resolution of the observations does not need to be very high because the generation of cross-talk between polarization states only requires a significant signal in the source polarization state. This offers the possibility to build up a data set with sufficient statistics over a time frame of weeks to months during periods of bad seeing.

In the same way that high spatial resolution is not ultimately required, there is also no requirement for observing active regions, pores or sunspots. Polarization amplitudes of a few percent in Stokes V are also reached by magnetic network elements (e.g., Rezaei et al. 2007). An accurate determination of the cross-talk between polarization states then only requires a high signal-to-noise ratio to detect a fraction of a percent-signal, i.e., signals of $10^{-4} - 10^{-3}$ amplitude must be above the noise floor.

Several of the spectral lines with or without negligible linear polarization signal that can be used for the application of the method (see Table 4 and Table 5) result from neutral atoms, unlike the singly-ionized line at 614.9 nm. The advantage of lines pertaining to neutral elements is that their line strength does not weaken in "cold" solar structures such as pores and sunspots, while singly-ionized lines can disappear completely exactly where the magnetic field strength and polarization signal is largest (see Fig. 7).

Although there is a dense wavelength coverage from the blue end of the visible spectrum at 400 nm up to 615 nm, there were no suitable lines found in the red end of the spectrum (> 615 nm).

8.2 Performance

As for most methods used to determine polarization properties, it is difficult to provide a good estimate of the accuracy of the approach. I find a residual $V \rightarrow QU$ cross-talk of about 3-10 % after application of the correction for the telescope polarization based on our 2016 best-fit values (Table 3). The residual cross-talk is comparable to that when using the 2010 telescope parameter set that was derived with a TCU. However, as seen in Figs. 14 and 17, there already is a significant scatter of a few percent in the input data that is presumably caused by residual interference fringes, and thus due to the quality of the input data, not the approach itself.

The values of the telescope parameters of my current determination match those of the 2010 telescope model within the error bars, however both are offset from literature values (Fig. 15). The match of the values determined from actual measurements at the DST is a positive sign, as the applicability of the literature values assuming thick coatings to the DST mirrors is not ensured. Therefore, based on my findings, I propose that this new calibration method is just as accurate as the standard DST calibration with a TCU.

9 Conclusions & Future Work

I conclude that it is possible to derive the parameters that describe the polarization properties of a telescope from observations of spectral lines with or without negligible linear polarization signal. These spectral lines cover much of the blue side of the visible part of the spectrum, but no suitable lines were found above 615 nm. Therefore, using spectral lines without linear polarization has proven to be a suitable tool to be used for the polarimetric calibration of large solar telescopes such as DKIST.

It is impossible to use a conventional TCU consisting of linear polarizers for the 4-m DKIST telescope. Using spectral lines without intrinsic linear polarization is thus a promising approach for its polarization calibration. At the DST, a time-dependent system with a variable geometric configuration has to be calibrated. The corresponding problem for DKIST is much less complex as only the first two mirrors need to be characterized which are static with fixed angles of incidence and a fixed relative orientation.

I would also like to search for suitable lines towards the red end of the spectrum and develop of a similar method to be used on lines with a regular Zeeman pattern, for which one will need to make either assumptions about the magnetic field geometry or the symmetry properties of Zeeman signals.

10 Acknowledgments

Thank you to my mentors Christian Beck and Valentin Pillet of the National Solar Observatory who made this project possible.

The National Solar Observatory is operated by the Association of Universities for Research in Astronomy, Inc. (AURA) under cooperative agreement with the National Science Foundation.

References

Beck, C., Schlichenmaier, R., Collados, M., Bellot Rubio, L., & Kentischer, T. 2005, A&A, 443, 1047

Cabrera Solana, D., Bellot Rubio, L. R., & del Toro Iniesta, J. C. 2005, A&A, 439, 687

Cavallini, F. 2006, Sol. Phys., 236, 415

Collados, M. 1999, in Astronomical Society of the Pacific Conference Series, Vol. 184, Third Advances in Solar Physics Euroconference: Magnetic Fields and Oscillations, ed. B. Schmieder, A. Hofmann, & J. Staude, 3–22

Dunn, R. B. 1964, Applied Optics, 3, 1353

Dunn, R. B. & Smartt, R. N. 1991, Advances in Space Research, 11, 139

Elmore, D. F., Lin, H., Socas Navarro, H., & Jaeggli, S. A. 2010, in Ground-based and Airborne Instrumentation for Astronomy III, Proc. SPIE, 7735, 77354E–77354E–6

Elmore, D. F., Lites, B. W., Tomczyk, S., et al. 1992, in Polarization Analysis and Measurement, ed. D. H. Goldstein & R. A. Chipman, Proc. SPIE, 1746, 22–33

Elmore, D. F., Sueoka, S. R., & Casini, R. 2014, in Ground-based and Airborne Instrumentation for Astronomy V, Proc. SPIE, 9147, 91470F

Harrington, D. M. & Sueoka, S. R. 2016, in Proc. SPIE, Vol. 9912, Advances in Optical and Mechanical Technologies for Telescopes and Instrumentation II, 99126U

Harrington, D. M. & Sueoka, S. R. 2017, ArXiv e-prints

Jaeggli, S. A., Lin, H., Mickey, D. L., et al. 2010, Mem. Soc. Astron. Italiana, 81, 763

Kurucz, R. L., Furenlid, I., Brault, J., & Testerman, L. 1984, Solar flux atlas from 296 to 1300 nm. National Solar Obs., Sunspot, New Mexico, ed. Kurucz, R. L., Furenlid, I., Brault, J., & Testerman, L.

Lites, B. W. 1993, Sol. Phys., 143, 229

McMullin, J. P., Rimmele, T. R., Warner, M., et al. 2016, in Society of Photo-Optical Instrumentation Engineers (SPIE) Conference Series, Proc. SPIE, 9906, 99061B

Reardon, K. P. & Cavallini, F. 2008, A&A, 481, 897

Rezaei, R., Schlichenmaier, R., Beck, C. A. R., Bruls, J. H. M. J., & Schmidt, W. 2007, A&A, 466, 1131

Ruiz Cobo, B. & del Toro Iniesta, J. C. 1992, ApJ, 398, 375

Sanchez Almeida, J. & Martinez Pillet, V. 1992, A&A, 260, 543

Sanchez Almeida, J. & Vela Villahoz, E. 1993, A&A, 280, 688

Schlichenmaier, R. & Collados, M. 2002, A&A, 381, 668

Schmidt, W., von der Lühe, O., Volkmer, R., et al. 2012, Astronomische Nachrichten, 333, 796

Selbing, J. 2010, ArXiv e-prints

Skumanich, A., Lites, B. W., Pillet, V. M., & Seagraves, P. 1997, ApJS, 110, 357

Socas-Navarro, H. 2005a, Journal of the Optical Society of America A, 22, 539

Socas-Navarro, H. 2005b, Journal of the Optical Society of America A, 22, 907

Socas-Navarro, H., Elmore, D., Asensio Ramos, A., & Harrington, D. M. 2011, A&A, 531, A2

Socas-Navarro, H., Elmore, D., Pietarila, A., et al. 2006, Sol. Phys., 235, 55

Socas-Navarro, H., Elmore, D. F., Keller, C. U., et al. 2005, in Solar Physics and Space Weather Instrumentation, ed. S. Fineschi & R. A. Viereck, Proc. SPIE, 5901, 52–59

Vela Villahoz, E., Sanchez Almeida, J., & Wittmann, A. D. 1994, A&AS, 103

A Appendix A: Line spectra at 426, 431 and 514 nm

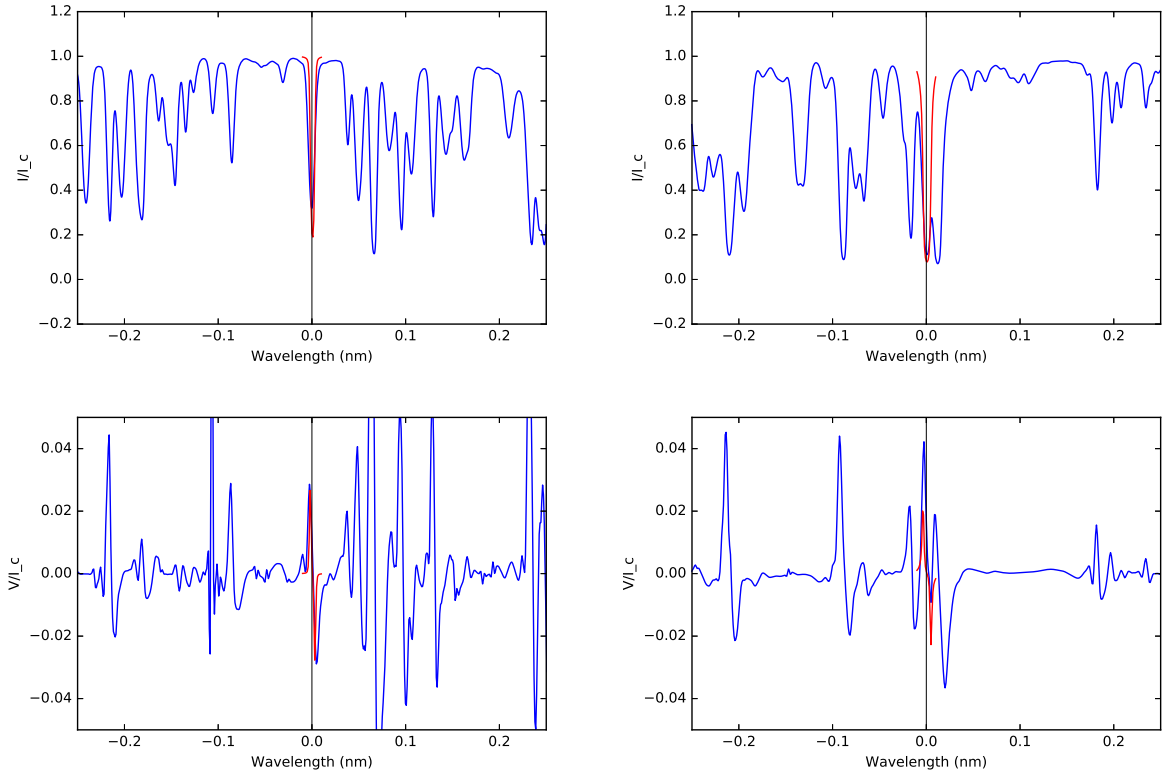

Figure 18: Synthetic Stokes profiles of Stokes I (top panel) and V (bottom panel) for the Mn I line at 425.766 nm (left column) and Ti II at 431.490 nm (right column) in the synthesis with 1500 G shown in red. The blue lines show the corresponding profiles from the FTS atlas.

Figures 18 and 19 show the profiles of the lines of Mn I at 425.766 nm (no LP), Ti II at 431.490 nm (no LP) and Fe I at 514.174 nm (small LP) from the synthesis with a magnetic field strength of 1500 G.

Corresponding example spectra from the observations are shown in Figs. 20 to 22. The Ti II line at 431.5 nm is partly blended with other Zeeman-sensitive lines. The residual fringe amplitude of still a few percent after removal of the strongest interference fringes makes any evaluation of the data at 425.8 nm and 431.5 nm unreliable. The observed peak Stokes V polarization amplitudes of both lines of about 0.1 are sufficient for the inference of telescope properties as demonstrated with the Ca I line at 526.2 nm that has a maximal Stokes V amplitude of 0.127. The Fe I line at 514.2 nm is well isolated in the spectrum (Figs. 19 and 22) and does not suffer strongly from interference fringes in the observations, but its wavelength range was already covered by the Ca I line at 526 nm, so we did not evaluate this data.

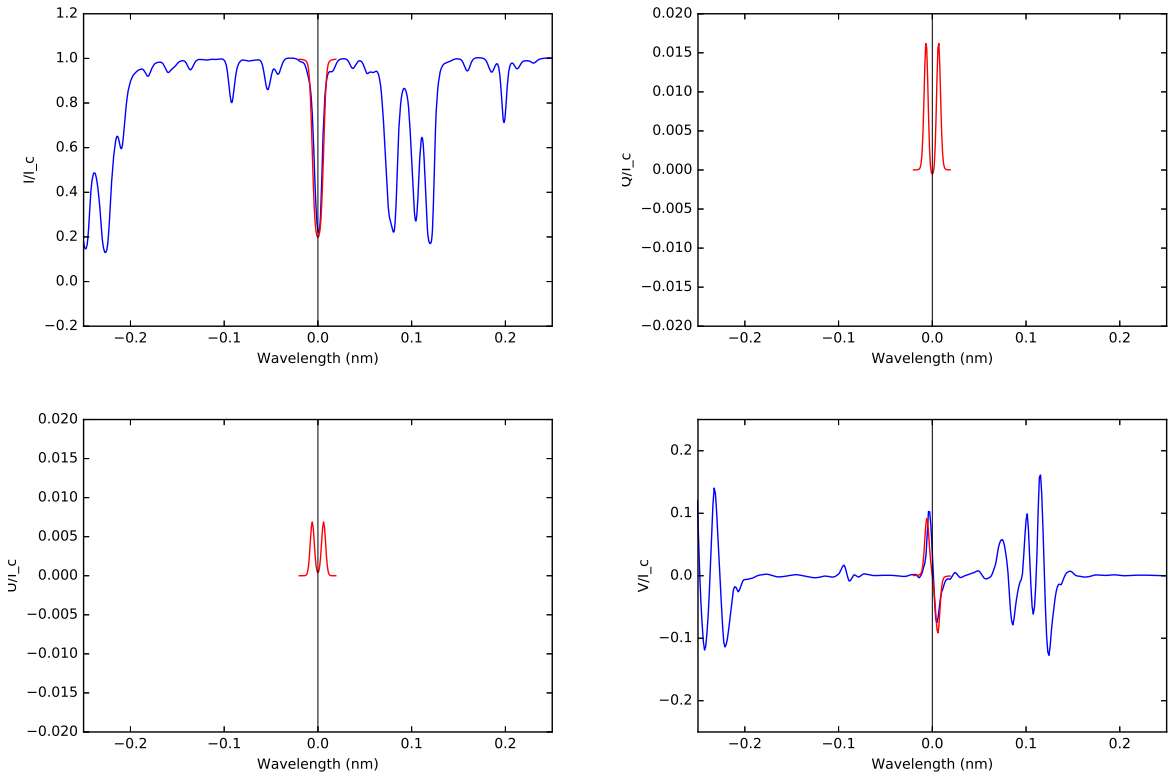

Figure 19: Synthetic Stokes profiles of Stokes I (top left), Q (top right), U (bottom left) and V (bottom right) for the Fe I line at 514.174 nm in the synthesis with 1500 G.

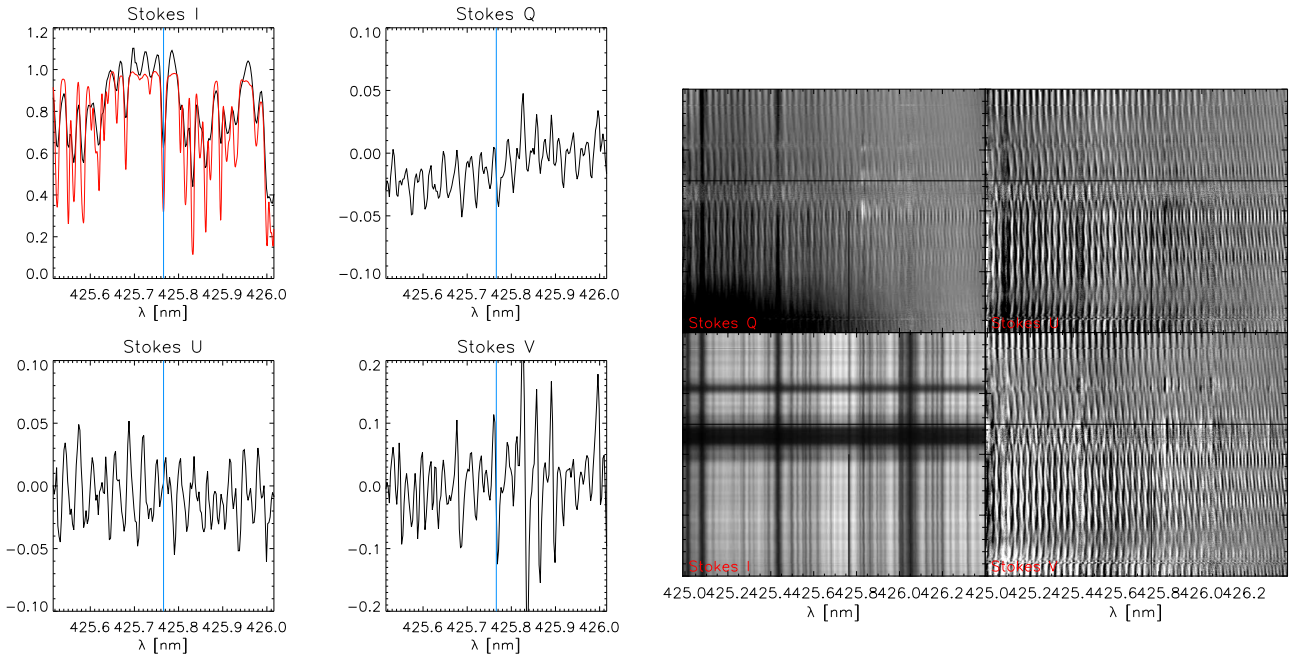

Figure 20: Example spectra of Mn I at 425.8 nm. Left four panels: individual $IQUV$ profiles from the location indicated with a horizontal black line in the right panels. The red line shows the corresponding profile from the FTS atlas. Right four panels: slit spectra of (clockwise, starting left bottom) $IQUV$ on a cut across the center of a sunspot. The line without LP is indicated by a black vertical bar.

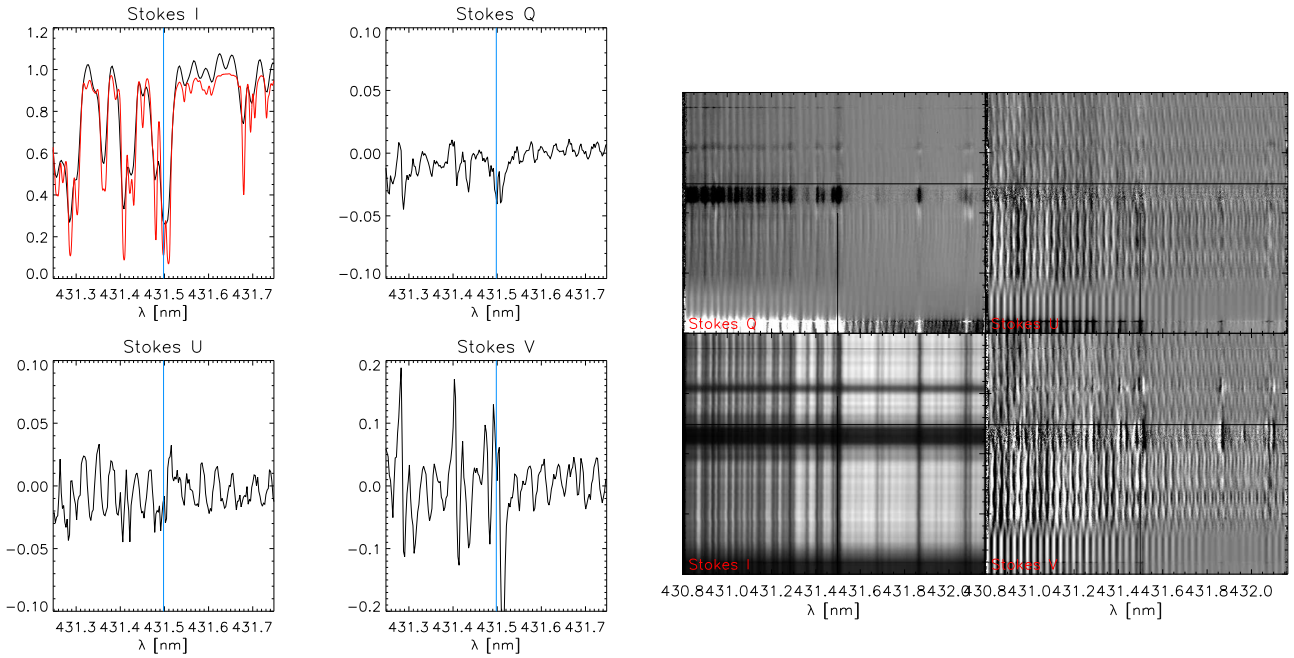

Figure 21: Same as Fig. 20 for Ti II at 431.5 nm.

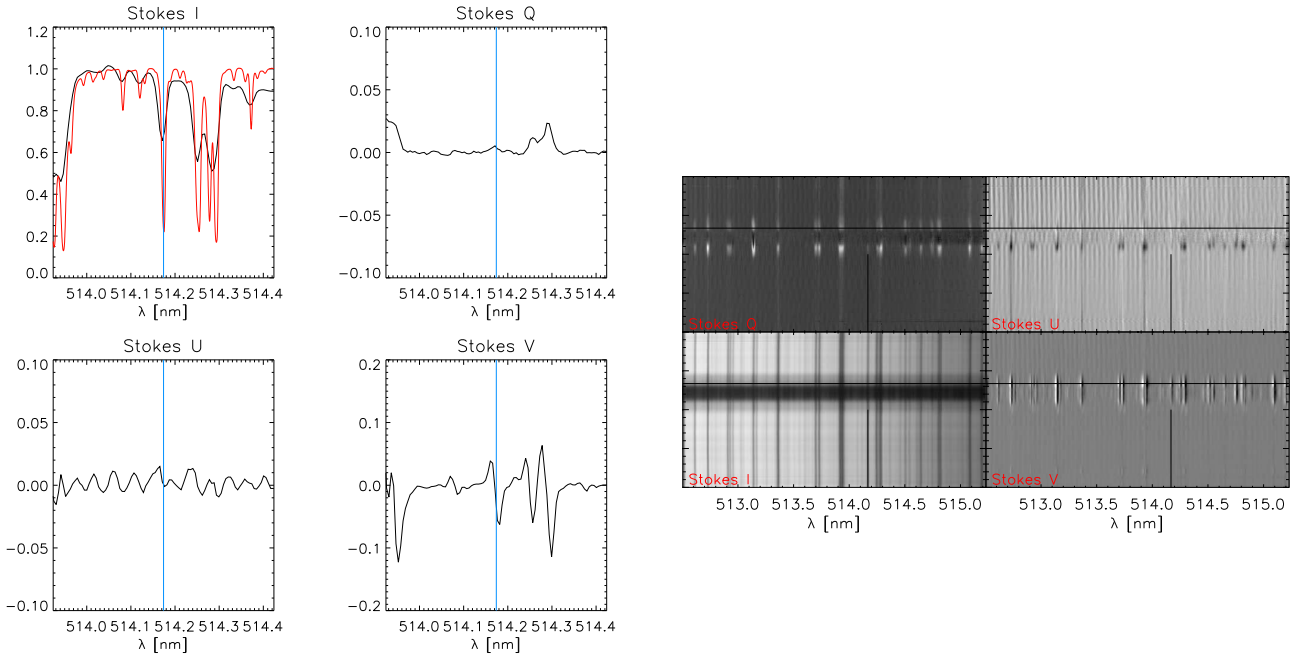

Figure 22: Same as Fig. 20 for Fe I at 514.2 nm.

B Appendix B: Transition parameters and polarization amplitude

Tables 4 and 5 contain the transition parameters and polarization amplitudes in the synthesis with 1500 G for all lines without and with small intrinsic linear polarization, respectively. All spectral lines for which the maximal Stokes V amplitude in the 1500 G synthesis is about 10 % or more are suitable for the inference of telescope properties as demonstrated with the Ca I line at 526.2 nm. For lines with lower polarization amplitudes, the problem reduces to the question whether the cross-talk is large enough that the spurious signals can still be measured in the observations. For the case of the DST, the $V \rightarrow QU$ cross-talk can be huge with values of T_{i4}/T_{44} above 1, but for other telescope that number can be as small as only a few percent. This implies that polarization signals at the $10^{-4} - 10^{-3}$ level have to be measured.

Table 4: Spectral lines without linear polarization. Transition parameters, minimal line-core intensity and maximal Stokes V polarization amplitudes at 1500 G.

Element	Ion. State	λ_0 [Å]	Excitation Potential (eV)	log (gf)	Transition	g_{eff}	min. I	max. $\|V/I\|$
Cr	II	4087.59	3.103	-3.22	4D 0.5- 6D 0.5	1.667	0.77028	0.07909
V	I	4093.5	1.183	-1.02	4P 0.5- 4D 0.5	1.333	0.92144	0.02739
V	I	4153.32	0.262	-2.55	6D 0.5-4D 0.5	1.667	0.98063	0.00708
Cu	I	4248.95	5.076	-0.976	4P 0.5- 4D 0.5	1.333	0.98631	0.00487
Mn	I	4257.66	2.953	-0.70	4D 0.5- 4P 0.5	1.333	0.18989	0.21631
S	II	4278.5	16.092	-0.11	4P 0.5- 4D 0.5	1.333	1.00043	2.6e-17
Ti	II	4314.9	1.1609	-1.104	4P 0.5- 4D 0.5	1.333	0.07868	0.15555
Fe	II	4385.38	2.778	-2.6	4P 0.5- 4D 0.5	1.333	0.12297	0.14503
Ti	II	4407.67	1.221	-2.617	2P 0.5- 4D 0.5	0.333	0.37181	0.07241
Ti	II	4411.93	1.224	-2.524	4P 0.5- 4D 0.5	1.333	0.32543	0.19735
S	II	4456.38	15.848	-0.55	4D 0.5- 4P 0.5	1.333	1.00015	1.2e-07
Cr	II	4588.20	4.071	-0.64	4D 0.5- 6F 0.5	0.333	0.18781	0.07415
V	I	4626.48	1.043	-1.24	4D 0.5- 4P 0.5	1.333	0.93216	0.02359
V	I	4757.48	2.029	-0.29	6G 1.5- 6F 0.5	0.167	0.93489	0.00456
Co	I	5247.93	1.785	-2.08	4P 0.5- 4D 0.5	1.333	0.75913	0.08375
Mn	I	5292.87	3.383	-2.90	4P 0.5- 4D 0.5	1.333	0.99262	0.00269
S	II	5473.62	13.584	-0.226	4P 0.5- 4D 0.5	1.333	1.00030	3.7e-06
C	II	5818.31	22.528	-1.464	4D 0.5- 4P 0.5	1.333	0.99982	9.9e-13
V	I	6008.67	1.183	-2.34	4P 0.5- 4D 0.5	1.333	0.99551	0.00142
V	I	6111.67	1.043	-0.715	4D 0.5- 4P 0.5	1.333	0.80069	0.06834
Co	I	6117.00	1.785	-2.49	4P 0.5- 4D 0.5	1.333	0.89543	0.03575
Fe	II	6149.23	3.889	-2.8	4D 0.5- 4P 0.5	1.333	0.54384	0.13369
S	II	6397.99	14.154	-0.791	4D 0.5- 4P 0.5	1.333	0.99974	2.4e-07
N	I	6646.50	11.750	-1.539	4D 0.5- 4P 0.5	1.333	1.00055	4.9e-05
C	II	6787.21	20.701	-0.377	4P 0.5- 4D 0.5	1.333	1.00038	9.7e-11
F	I	6870.22	12.751	-0.27	4P 0.5- 4D 0.5	1.333	1.00011	5.6e-08
Co	I	6872.40	2.008	-1.85	4P 0.5- 4D 0.5	1.333	0.76954	0.08110
Cl	I	8428.25	9.029	-0.29	4P 0.5- 4D 0.5	1.333	0.99912	0.00046
N	I	8703.25	10.326	-0.310	4P 0.5- 4D 0.5	1.333	0.97682	0.00858
P	I	10596.90	6.935	-0.24	4P 0.5- 4D 0.5	1.333	0.94471	0.01941
N	I	11294.26	11.750	-0.531	4D 0.5- 4P 0.5	1.333	0.99809	0.00062

Table 5: Spectral lines with small linear polarization. Transition parameters and maximal Stokes QUV/I polarization amplitudes at 1500 G.

Elem.	Ion. State	λ_0 [Å]	Excit. Pot. (eV)	log (gf)	Transition	g_{eff}	max. $\lvert Q/I\rvert$	max. $\lvert U/I\rvert$	max. $\lvert V/I\rvert$
Ti	I	4005.95	2.103	-0.53	5F 3.0- 5H 4.0	0.375	0.00025	0.00025	0.02517
Fe	I	4007.27	2.759	-1.276	3G 3.0- 3F 2.0	0.500	0.01040	0.02621	0.20485
Fe	I	4017.08	2.759	-1.992	3G 3.0- 3D 2.0	0.333	0.00338	0.00510	0.12080
He	I	4026.19	20.96	-1.453	3P 1.0- 3D 1.0	1.000	1.2e-09	1.2e-09	1.2e-07
Fe	I	4076.22	3.071	-1.99	3P 1.0- 3D 1.0	1.000	0.00743	0.01482	0.2171
Fe	I	4109.80	2.845	-0.940	3P 1.0- 3D 1.0	1.000	0.00022	0.00433	0.11059
Co	I	4132.14	1.049	-2.82	2F 2.5- 4D 2.5	1.114	0.00212	0.00199	0.06178
Al	II	4227.95	15.062	-1.709	3D 2.0- 3F 2.0	0.917	1.1e-09	1.1e-09	4.9e-08
Fe	I	4229.51	3.274	-1.628	3D 1.0- 3P 1.0	1.000	0.00782	0.01728	0.21710
Cr	I	4232.23	4.207	-0.50	3D 2.0- 3G 3.0	0.333	9.9e-05	9.7e-05	0.01093
Fe	II	4296.57	2.704	-2.9	4P 1.5- 4F 2.5	0.500	0.00579	0.01172	0.12746
Cl	II	4304.04	15.712	-0.68	3D 1.0- 3P 1.0	1.000	1.9e-12	1.9e-12	9.6e-11
Sc	II	4305.71	0.595	-1.30	3F 2.0- 3D 2.0	0.917	0.00252	0.00369	0.11599
Cr	I	4312.47	3.113	-1.37	3F 3.0- 3H 4.0	0.375	0.00039	0.00038	0.01733
Fe	I	4367.90	1.608	-2.886	3F 2.0- 5G 2.0	0.500	0.00019	0.00027	0.08157
Cr	I	4410.96	2.983	-1.22	3H 5.0- 5F 4.0	0.400	0.00061	0.00060	0.02623
Fe	I	4422.57	2.845	-1.115	3P 1.0- 3D 1.0	1.000	0.00165	0.01134	0.19642
Cr	I	4429.92	3.556	-0.67	3D 1.0- 3P 1.0	1.000	0.00144	0.00132	0.06407
Ca	I	4435.69	1.886	-0.519	3P 1.0- 3D 1.0	1.000	0.00014	0.00544	0.10952
He	I	4471.48	20.964	-1.036	3P 1.0- 3D 2.0	1.000	9.9e-09	9.9e-09	2.1e-07
Ni	I	4513.0	3.706	-1.47	3D 2.0- 3F 2.0	0.917	0.00216	0.00233	0.08957
Cr	II	4539.59	4.0423	-2.53	2F 2.5- 4D 2.5	1.114	0.00121	0.00115	0.04112
Al	II	4589.67	15.062	-1.608	3D 2.0- 3F 2.0	0.917	1.2e-09	1.2e-09	4.8e-08
P	II	4626.70	12.812	-0.32	3D 2.0- 3F 2.0	0.917	4.9e-09	4.9e-09	2.0e-07
Cr	I	4698.94	3.079	-1.44	3G 3.0- 3D 2.0	0.333	0.00018	0.00017	0.01415
Ti	I	4722.61	1.053	-1.33	3P 1.0- 3D 1.0	1.000	0.00271	0.00243	0.09725
C	I	4738.21	7.946	-3.115	3D 1.0- 3P 1.0	1.000	4.5e-05	4.5e-05	0.00249
Cr	I	4767.27	3.556	-1.02	3D 2.0- 3F 2.0	0.917	0.00069	0.00066	0.03075
Cl	II	4778.91	17.086	-0.35	3P 1.0- 3D 1.0	1.000	3.1e-13	3.08e-13	0.04350
Ni	I	4808.87	3.706	-1.41	3D 2.0- 3G 3.0	0.333	0.00069	0.00066	0.04350
Fe	I	4813.11	3.274	-2.84	3D 1.0- 5D 1.0	1.000	0.00349	0.00309	0.10193
Si	I	4823.32	4.930	-2.33	3P 1.0- 3D 1.0	1.000	0.00109	0.00116	0.06830
Fe	II	4833.19	2.657	-4.8	4H 5.5- 6F 4.5	0.455	0.00067	0.00066	0.02097
Sr	I	4876.08	1.798	-0.551	3P 1.0- 3D 1.0	1.000	0.00026	0.00026	0.00424
Cl	II	4922.15	15.714	-0.59	3D 2.0- 3F 2.0	0.917	1.4e-12	1.4e-12	5.8e-11
Cl	II	4924.25	15.626	-1.54	3F 2.0- 3D 2.0	0.917	1.8e-13	1.8e-13	7.4e-12
P	II	4927.20	12.791	-0.68	3D 1.0- 3P 1.0	1.000	1.5e-09	1.5e-09	8.1e-08
Fe	I	4930.32	3.960	-1.201	3D 1.0- 5D 1.0	1.000	0.00309	0.00589	0.13024
Cr	I	4936.34	3.113	-0.34	3F 3.0- 3H 4.0	0.375	0.00221	0.00252	0.08351
Ti	I	4941.57	2.160	-1.01	3D 2.0- 3F 2.0	0.917	0.00047	0.00046	0.02019
Ti	I	4997.09	0.000	-2.056	3F 2.0- 3D 2.0	0.917	0.00432	0.00508	0.14870
Fe	I	5021.59	4.256	-0.677	5F 3.0- 5H 4.0	0.375	0.00418	0.00647	0.11272
Fe	I	5099.08	3.984	-1.265	3F 2.0- 3D 2.0	0.917	0.00313	0.00542	0.12185
Fe	I	5141.74	2.424	-2.238	3P 1.0- 3D 1.0	1.000	0.00305	0.01106	0.13839

Table 6: Spectral lines with small linear polarization cont.

Elem.	Ion. State	λ_0 [Å]	Excit. Pot. (eV)	log (gf)	Transition	g_{eff}	max. $\|Q/I\|$	max. $\|U/I\|$	max. $\|V/I\|$
Fe	I	5207.94	3.635	-2.40	3D 1.0- 3P 1.0	1.000	0.00485	0.00421	0.11170
Ca	I	5261.71	2.521	-0.73	3D 1.0- 3P 1.0	1.000	0.00315	0.00790	0.12739
Al	II	5280.27	15.586	-1.981	3P 1.0- 3D 1.0	0.917	1.1e-10	1.1e-10	6.0e-09
Ti	I	5300.01	1.053	-1.47	3P 1.0- 3D 1.0	1.000	0.00294	0.00274	0.07535
C	I	5300.87	8.640	-2.622	3D 1.0- 3P 1.0	1.000	3.7e-05	3.7e-05	0.00194
Fe	I	5341.02	1.608	-1.953	3F 2.0- 3D 2.0	0.917	0.00139	0.00614	0.12045
Ni	I	5353.39	1.951	-2.81	3P 1.0- 3D 1.0	1.000	0.00824	0.00782	0.15667
Ni	I	5514.79	3.847	-1.99	1F 3.0- 3P 2.0	0.500	0.00048	0.00047	0.01521
Fe	I	5667.66	2.609	-2.94	3F 2.0- 3D 2.0	0.917	0.00253	0.00357	0.11359
Fe	I	5747.95	4.608	-1.41	3F 3.0- 3H 4.0	0.375	0.00137	0.00147	0.05643
Fe	I	6085.26	2.759	-2.712	3G 3.0- 3D 2.0	0.333	0.00284	0.00332	0.09539
Fe	I	6127.91	4.413	-1.399	3F 3.0- 3H 4.0	0.375	0.00209	0.00245	0.07114